Geophysical Journal International

Geophys. J. Int. (2022) **230,** 29–49
Advance Access publication 2022 February 11
GJI Seismology

https://doi.org/10.1093/gji/ggac042

Spectral element numerical simulation of the 2009 L'Aquila earthquake on a detailed reconstructed domain

F. Di Michele,[1] J. May,[2] D. Pera,[2] V. Kastelic,[3] M. Carafa,[3] C. Smerzini,[4] I. Mazzieri,[5] B. Rubino,[2] P.F. Antonietti,[5] A. Quarteroni,[5,6,*] R. Aloisio[1,7] and P. Marcati[1]

[1]*Gran Sasso Science Institute (GSSI), via M. Iacobucci* 2, *I*-67100 *L'Aquila, Italy. E-mail: pierangelo.marcati@gssi.it*
[2]*Department of Information Engineering, Computer Science and Mathematics, University of L'Aquila, via Vetoio, loc. Coppito, I*-67100 *L'Aquila, Italy*
[3]*Istituto Nazionale di Geofisica e Vulcanologia, Sezione Tettonofisica e Sismologia, L'Aquila, I-67100, Italy*
[4]*Department of Civil and Environmental Engineering, Politecnico di Milano, Piazza L. da Vinci* 32, I-20133 *Milan, Italy*
[5]*MOX—Dipartimento di Matematica, Politecnico di Milano, P.zza Leonardo da Vinci* 32, *I*-20133 *Milan, Italy*
[6]*Mathematics Institute, École Polytechnique Fédérale de Lausanne, Av. Piccard, CH*-1015 *Lausanne, Switzerland*
[7]*INFN—Laboratori Nazionali del Gran Sasso, Via G. Acitelli* 22, *Assergi (AQ), I-67100, Italy*

Accepted 2022 February 3. Received 2022 January 7; in original form 2021 March 12

SUMMARY

In this paper, we simulate the earthquake that hit the city of L'Aquila on 2009 April 6 using SPEED (SPectral Elements in Elastodynamics with Discontinuous Galerkin), an open-source code able to simulate the propagation of seismic waves in complex 3-D domains. Our model includes an accurate 3-D reconstruction of the Quaternary deposits, according to the most up-to-date data obtained from the Microzonation studies in Central Italy and a detailed model of the topography incorporated using a newly developed tool. The sensitivity of our results with respect to different kinematic seismic sources is investigated. The results obtained are in good agreement with the recordings at the available seismic stations at epicentral distances within a range of 20 km. Finally, a blind source prediction scenario application shows that a reasonably good agreement between simulations and recordings can be obtained by simulating stochastic rupture realizations with basic input data. These results, although limited to nine simulated scenarios, demonstrate that it is possible to obtain a satisfactory reconstruction of a ground shaking scenario employing a stochastic source constrained on a limited amount of ex-ante information. A similar approach can be used to model future and past earthquakes for which little or no information is typically available, with potential relevant implications for seismic risk assessment.

Key words: Computational seismology; Earthquake ground motions; Earthquake hazards; Site effects; Wave propagation; Neotectonics.

1 INTRODUCTION

Seismic damage and loss scenarios in large urban areas represent a key tool for civil protection planning to improve earthquake preparedness, establish effective prevention policies for seismic risk mitigation and support decision making in emergency management. To accomplish this task, a realistic estimation of earthquake ground motion and its spatial distribution during simulated earthquakes is essential, especially in the case of complex urban environments located close to seismically active faults. It is recognized that the coupling of seismic source features, geomorphological structures and local site conditions may have a dramatic influence in determining an uneven spatial distribution of ground shaking and, therefore, the observed damage for homogeneous vulnerability conditions (Kawase 1996; Assimaki *et al.* 2012; Gallipoli *et al.* 2012). The standard approach for producing ground shaking scenarios during possible future earthquakes is the empirical approach, based on the use of ground motion prediction equations (GMPEs). GMPEs are statistical regressions on data sets of ground motion recordings, providing estimates of the probability distribution of ground motion intensity measures (e.g. peak ground acceleration—PGA), as a function

*Professor Emeritus

© The Author(s) 2022. Published by Oxford University Press on behalf of The Royal Astronomical Society. This is an Open Access article distributed under the terms of the Creative Commons Attribution License (https://creativecommons.org/licenses/by/4.0/), which permits unrestricted reuse, distribution, and reproduction in any medium, provided the original work is properly cited.

Downloaded from https://academic.oup.com/gji/article/230/1/29/6526874 by INGV user on 22 June 2022

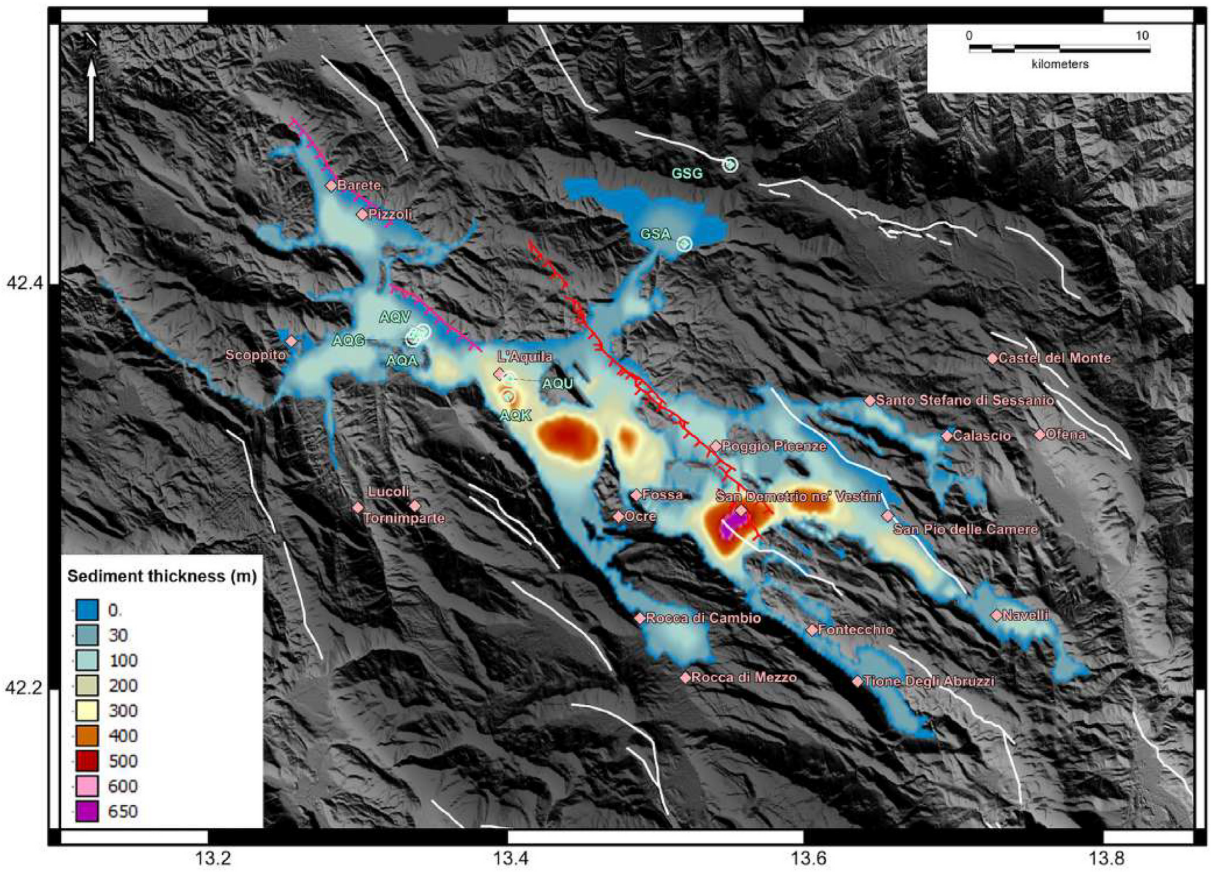

Figure 1. Map of the Quaternary L'Aquila–San Demetrio sedimentary basin. The white polylines represent local active faults (from Carafa *et al.* 2020). The red (Paganica–San Demetrio) and magenta (Pizzoli–Mt Marine) are active faults that are discussed in Section 2.1. The green textured circles represent the seismic stations used in the analyses (from Table 2). For more details, see the text.

Table 1. Crustal model coefficients.

Layer	Depth (km)	V_S (m s^{-1})	V_P (m s^{-1})	ρ (g cm^{-3})	Q
1	1	1700	3160	2.5	100
2	1	2600	4380	2.5	200
3	3	3100	5760	2.84	200
4	15	3500	6510	3.18	200

of explanatory variables, such as magnitude, distance and site conditions. GMPEs are routinely used in engineering practice but suffer because of the scarcity of data in the near-source region of severe earthquakes, the unsuitability to account for the specificity of the geological conditions and the spatial variability of ground motion. More recently, thanks to the enormous computational capabilities made available by high-performance parallel computers, 3-D physics-based mathematical models have been extensively used to generate earthquake scenarios that account for the fault rupture and complexity of regional or local geological conditions (Burstedde *et al.* 2013; Breuer *et al.* 2014; Galvez *et al.* 2014; Petersson & Sjögreen 2018; van Zelst *et al.* 2019; Infantino *et al.* 2020; Paolucci *et al.* 2021a). These models rely on the numerical solution of the visco-elastodynamic equations in complex heterogeneous media with *high-order* and *flexible* computational methods, such as the spectral element method (SEM) in either its continuous or discontinuous form, the ADER-DG method and the finite-difference method to cite a few (Dumbser *et al.* 2007; Moczo *et al.* 2011, 2014; Pelties *et al.* 2012; Chaljub *et al.* 2015; Antonietti *et al.* 2018; Duru *et al.* 2020; Wolf *et al.* 2020).

Because of the intrinsically high epistemic uncertainties involved in the construction of 3-D numerical models, those need to be verified and validated against available earthquake recordings (Bielak *et al.* 2010; Paolucci *et al.* 2015, 2021b).

It is worth recalling that, owing to the considerable increase of earthquake recordings, state-of-the-art GMPEs begin to remove the ergodic assumption (i.e. equivalence between the distribution of the random variable in space and the distribution of the same variable at a single point when sampled over time) and, therefore, to mimic the physics-based simulations, by adjusting the model coefficients based on region-specific earthquake, path and site observed effects (Kotha *et al.* 2020; Sgobba *et al.* 2021). In this paper, the case study of the M_w 6.1 2009 April 6 earthquake, which struck the city of L'Aquila (Abruzzo, Italy) causing 309 deaths and more than 1600 injuries, is addressed.

Downloaded from https://academic.oup.com/gji/article/230/1/29/6526874 by INGV user on 22 June 2022

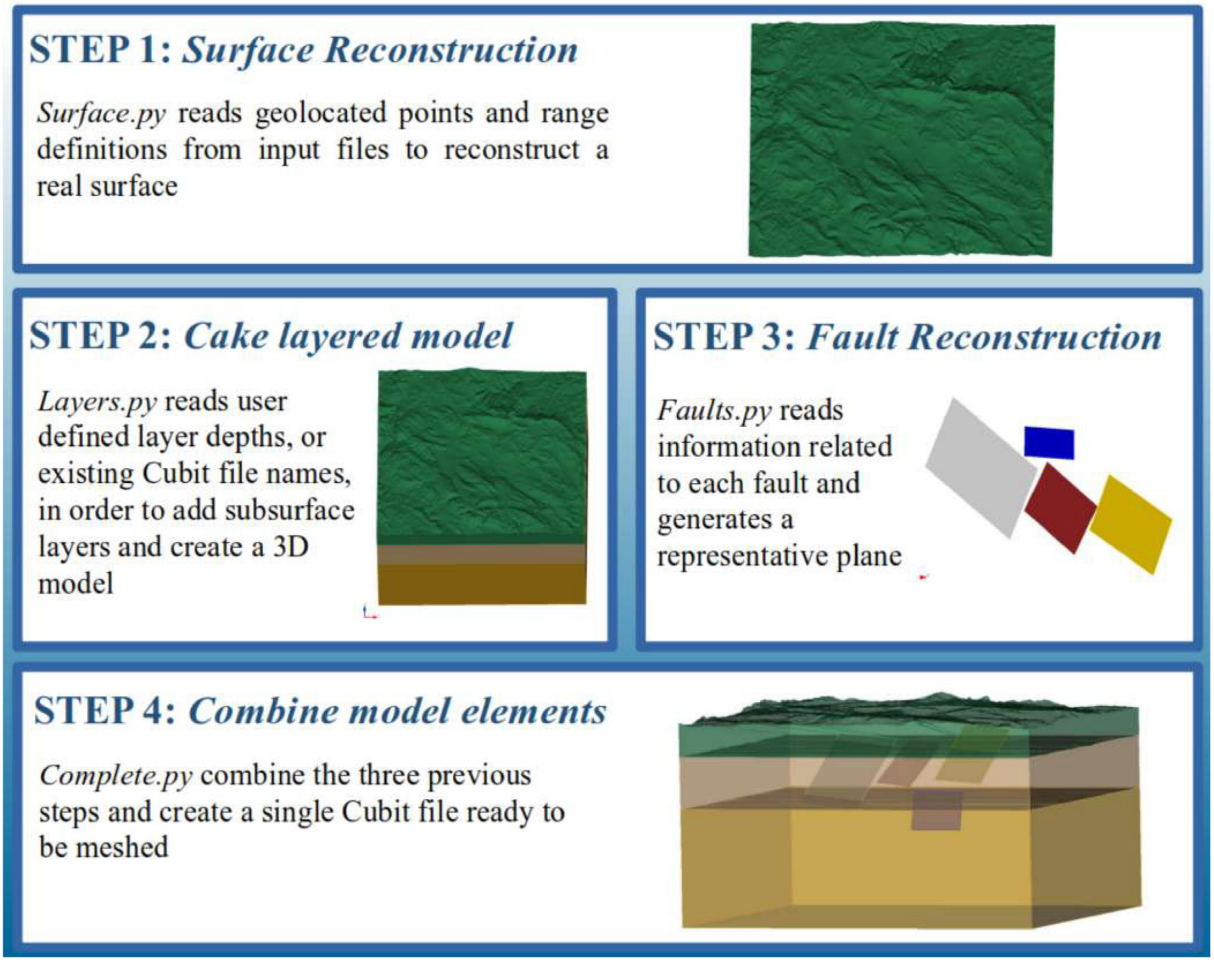

Figure 2. Schematic description of the Python scripts workflow.

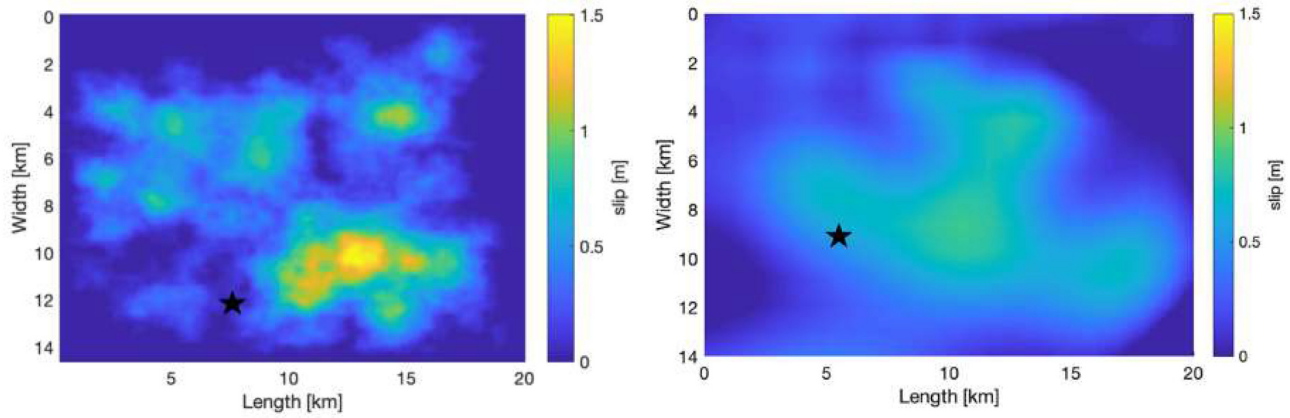

Figure 3. Slip distribution on the implemented co-seismic fault plane for *Model 1* (left) and *Model 2* (right).

L'Aquila was partially destroyed and so were many surrounding towns and villages. The main seismic event was preceded by a long sequence of foreshocks (Sugan *et al.* 2014) and followed by hundreds of aftershocks, the largest of which occurred on 2009 April 7 with a magnitude of 5.6. For this reason, a dense set of seismic instruments was activated within the region, providing a unique amount of data in terms of number and quality (Ameri *et al.* 2009; Magnoni *et al.* 2013; Zambonelli *et al.* 2017), which was used to build relatively few 3-D physics-based numerical simulations of the main event (*cf.* Smerzini & Villani 2012; Magnoni *et al.* 2013; Evangelista *et al.* 2017).

In Magnoni *et al.* (2013), the authors reconstructed a large 3-D domain that extends for 200 km in the directions north–south (N–S) and east–west (E–W), with a depth of 60 km. The Moho discontinuity and the main basins, such as Aterno and Fucino valleys, were included. Simulations were made using SPECFEM3D_Cartesian software (Komatitsch *et al.* 2004; Tromp *et al.* 2008; Peter *et al.* 2011) and the

Downloaded from https://academic.oup.com/gji/article/230/1/29/6526874 by INGV user on 22 June 2022

Model	*Fault Solution*	*Mw*	*Slip distribution*	*Mesh Features*	*Domain Image*
Model 1	L = 28 km W = 20.9 km Strike = 133° Dip = 54° Rake = -102°	6.1	1	Size = (59.5, 57.5, 19.8) km No. Elements = 776426 Spectral Degree = 3 No. mesh nodes = 803222 Δt = 0.0005s Duration = 30s	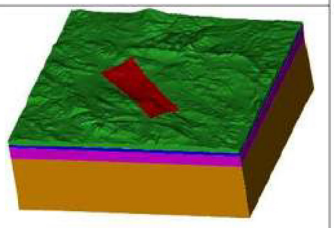
Model 2	L = 20 km W = 14 km Strike = 133.5° Dip = 47° Rake = -103.5°	6.3	1	Size = (65.9, 57.8, 19.8) km No. Elements = 3762721 Spectral Degree = 3 No. mesh nodes = 4088818 Δt = 0.00025s Duration = 30s	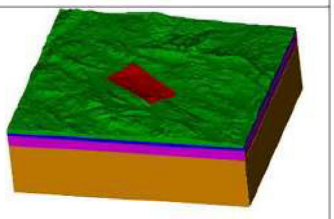
Paganica Prediction	L = 14 km W = 9.5 km Strike = 127° Dip = 50° Rake = 270°	6.1 6.2 6.3	3 (hypothetical) 3 (hypothetical) 3 (hypothetical)	Size = (65.9, 57.8, 19.8) km No. Elements = 1715476 Spectral Degree = 3 No. mesh nodes = 1865398 Δt = 0.00025s Duration = 30s	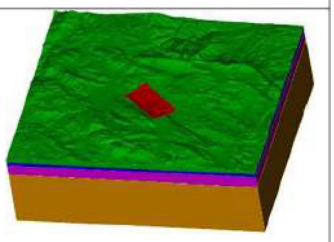

Figure 4. Description of the three computational domains, labelled as *Model 1*, *Model 2* and blind prediction. For each of them, size, mesh properties, related fault plane and the magnitude of the simulate earthquake(s) are displayed. Each fault projection is shown in red.

Table 2. Position of the seismic stations, in terms of geographic coordinates, Lat(°N)–Long (°E), and epicentral distance (R_e).

Siesmic stations ID	Lat (°)	Long (°)	R_e (km)
AQK	42.3449	13.4009	1.8
AQU	42.3538	13.4019	2.2
AQV	42.3772	13.3438	4.9
AQG	42.3734	13.3370	5.0
AQA	42.3755	13.3392	5.0
GSA	42.4206	13.5193	14.4
GSG	42.4600	13.5500	19.2

kinematic sources were taken from Cirella *et al.* (2009). These results were in good agreement with the 27 recorded signals in the frequency range of 0.02−0.5 Hz.

In Smerzini & Villani (2012), the same earthquake was simulated on a domain with dimensions around 62 km in N–S and E–W directions and 20 km depth. Numerical results were obtained with GeoELSE (Stupazzini *et al.* 2009) by comparing four kinematic sources coming from the inversion of seismic data, at frequencies up to 2.5 Hz. As in the previous case, the synthetic seismographs were compared to the recorded data, and a fairly good agreement was observed. More recently, Evangelista *et al.* (2017) simulated the 2009 April 9 earthquake using a comparable domain and a similar approach as in Smerzini & Villani (2012), using a more recently developed library named SPEED that is based on a discontinuous Galerkin spectral element paradigm (Antonietti *et al.* 2012; Mazzieri *et al.* 2013). The more accurate reconstruction of the alluvial basin and of the kinematic source allows for a better agreement with the recorded data with respect to Smerzini & Villani (2012).

In this work, we present a new set of numerical simulations of the L'Aquila event, using the same numerical code SPEED. Some improvements were made to the pre-processing MATLAB scripts in order to correctly handle the newer versions of the exodus file type, seen in (at least) Trelis 16.3 (now Coreform Cubit, `https://coreform.com/products/coreform-cubit`). The new numerical model of the L'Aquila area was obtained by focusing on the following aspects: (i) the subsoil reconstruction, with emphasis on the Middle Aterno Valley—a Quaternary sedimentary basin—on which L'Aquila town is built; (ii) the topography reconstruction with inclusion of high mountains and canyons that could influence wave propagation; and finally (iii) the influence of the kinematic source. Comparing with the models available in the literature (Smerzini & Villani 2012; Magnoni *et al.* 2013; Evangelista *et al.* 2017), our reconstructed domain follows the geological and morphological characteristics of the investigated area with a higher accuracy. To create the topography of the computational domain, we

Downloaded from https://academic.oup.com/gji/article/230/1/29/6526874 by INGV user on 22 June 2022

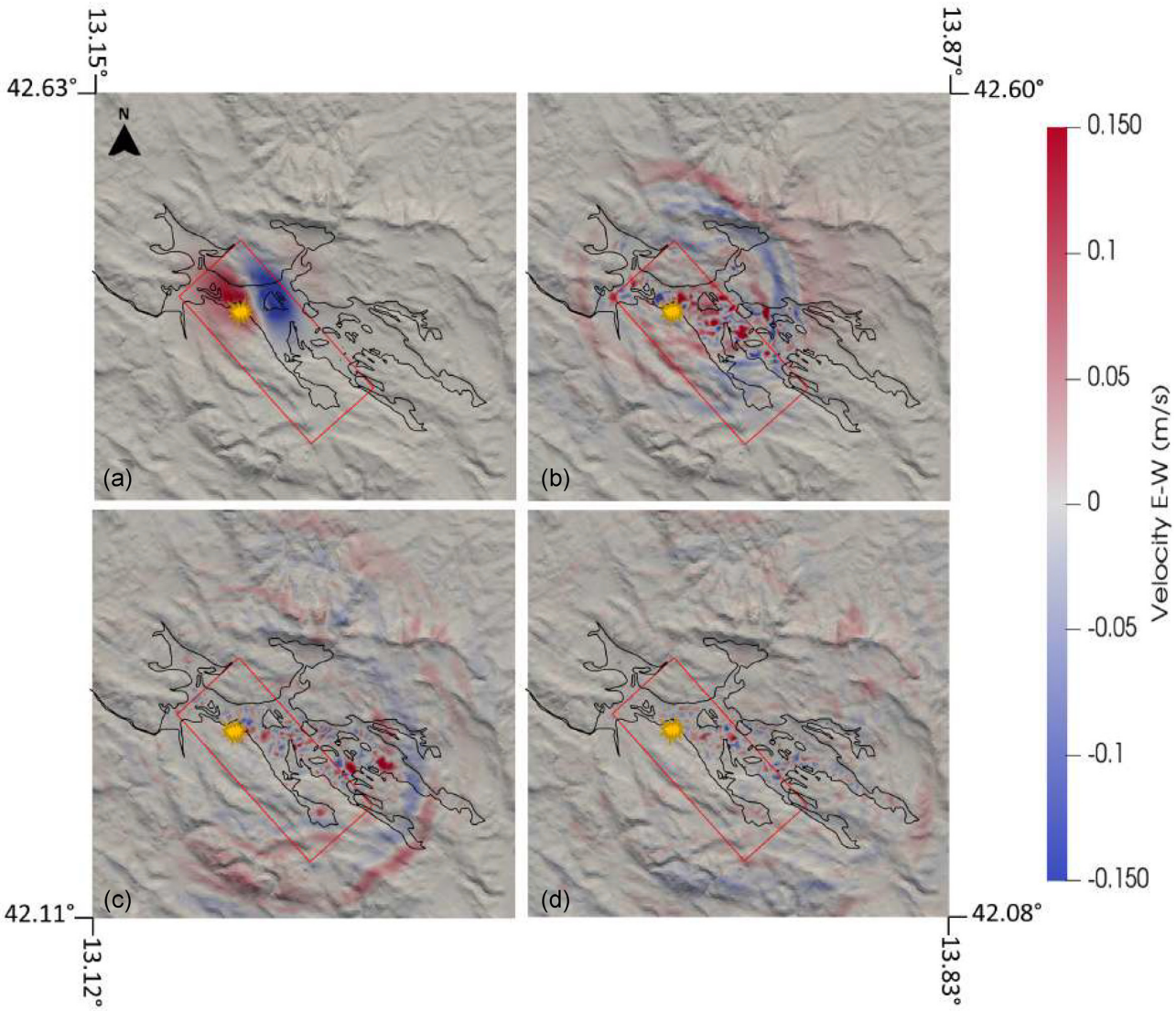

Figure 5. Velocity in the E–W direction (m s^{-1}) for *Model 1* at 6, 10, 16 and 20 s (a–d, respectively).

started from a 10 m resolution DEM provided by the TINITALY project (see Tarquini *et al.* 2007, 2012; Tarquini & Nannipieri 2017, for more details) and, using a new software tool, *cf.* May *et al.* (2021), we achieved a highly accurate reconstruction. This procedure requires minimal user input and interfaces directly with the Trelis/Cubit software. The importance of using an accurate topography has been emphasized in Magnoni *et al.* (2013) and in many other papers; see, for example, Bouchon *et al.* (1996), Bouchon & Barker (1996), Durand *et al.* (1999) and Lee *et al.* (2009).

The influence of the kinematic seismic source on earthquake ground motions in the near-source region is explored by considering both the source inversion models presented in Atzori *et al.* (2009), Ameri *et al.* (2012) and Evangelista *et al.* (2017) and sources computed with the stochastic rupture generator by Schmedes *et al.* (2013).

The paper is organized as follows. In Section 2, we describe the domain creation procedure and present the geological setting on which the computational domain is built, emphasizing the contribution to the available literature. In Section 3, we discuss the effect of different seismic sources for the simulation of 2009 April 6 L'Aquila earthquake. In particular, we compare two kinematic sources obtained by different techniques for seismic source inversion. Results of the simulations are discussed and the comparison with the available recorded data is shown. Finally, in Section 4, we perform a 'blind prediction' exercise. To this end, the 2009 earthquake is simulated using a stochastic co-seismic slip distribution (Schmedes *et al.* 2013), across an assigned fault plane according to the Database of Individual Seismogenic Sources (DISS, `http://diss.rm.ingv.it/dissGM/`). The comparison between the synthetic scenarios and recorded data is addressed, in order to evaluate the prediction capability of the simulations with a source model constrained on a limited input information. In the final section, we draw some conclusions and illustrate possible future developments of this work.

Downloaded from https://academic.oup.com/gji/article/230/1/29/6526874 by INGV user on 22 June 2022

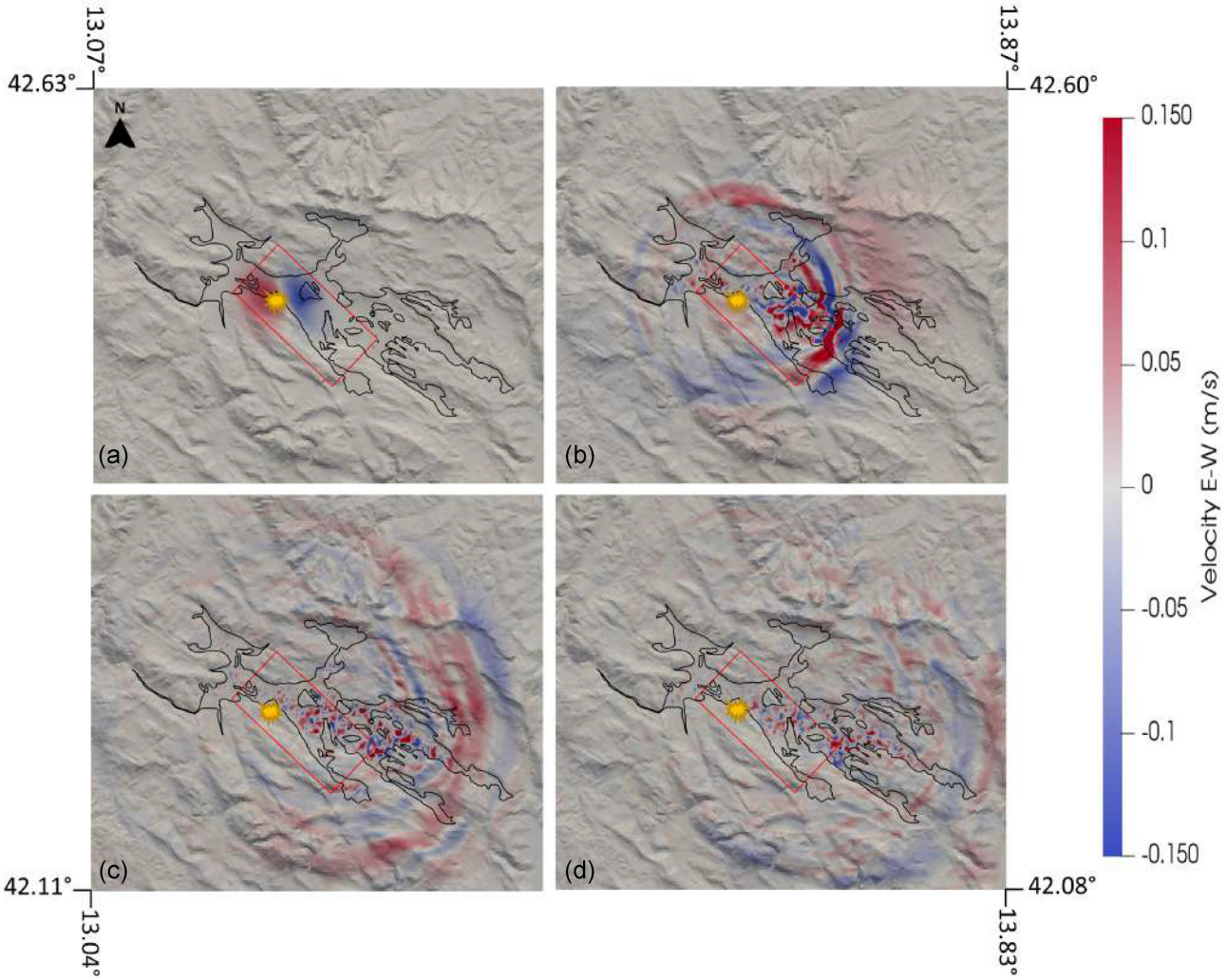

Figure 6. Velocity in the E–W direction (m s^{-1}) for *Model 2* at 4, 8, 14 and 18 s (a–d, respectively).

2 SIMULATION DESIGN: GEOLOGICAL SETTING AND COMPUTATIONAL DOMAIN CONSTRUCTION

In this section, we show the construction of the computational model, obtained starting from a detailed topography reconstruction and a large-scale 3-D model of the Quaternary-infill of the area of interest. Moreover, we present a new tool able to simplify and speed up the construction of the computational mesh, *cf.* May *et al.* (2021).

2.1 Geologic setting and Quaternary basin reconstruction

It is well known that the basin geometry and its overall structure and composition influence the lateral variations in peak earthquake ground motion, amplification and shaking duration (Gutenberg 1957; De Luca *et al.* 2005; Ewald *et al.* 2006). As the scope of the present work is to reproduce the ground shaking in a given area as accurately as possible, we strive to include in our numerical model not only realistic seismic sources but also a detailed reconstruction of the submerged morphology of the territory. With respect to the previous works that consider the same study area (e.g. Smerzini & Villani 2012; Evangelista *et al.* 2017), we aimed to construct a more spatially and geometrically comprehensive numerical model based on numerous geologic, geophysical and geomorphologic data.

Our study area is situated in the central Apennines, a mountain chain characterized by post-collisional seismogenic active extension predominantly expressed along NW–SE striking normal faults and by regional-scale uplift. The seismogenic normal faults rejuvenate the older compressional tectonic-related setting (e.g. Patacca & Scandone 1989) and affect the Meso-Cenozoic carbonate and partially terrigenous rocks, while their activity controls the deposition and deformation of Quaternary sediments in their form of basin infill (e.g. Bosi 1989; Centamore *et al.* 2010). The typical morphology of the central Apennines consists of individual NW–SE oriented mountain fronts and intermediary high karstic plateaus intermittent with inter-mountain basins and fluvial-glacial valleys. Such morphology is the outcome of different tectonic phases that affected the area during its geological evolution (Bertini & Bosi 1976), as well as effects of gravity driven

Downloaded from https://academic.oup.com/gji/article/230/1/29/6526874 by INGV user on 22 June 2022

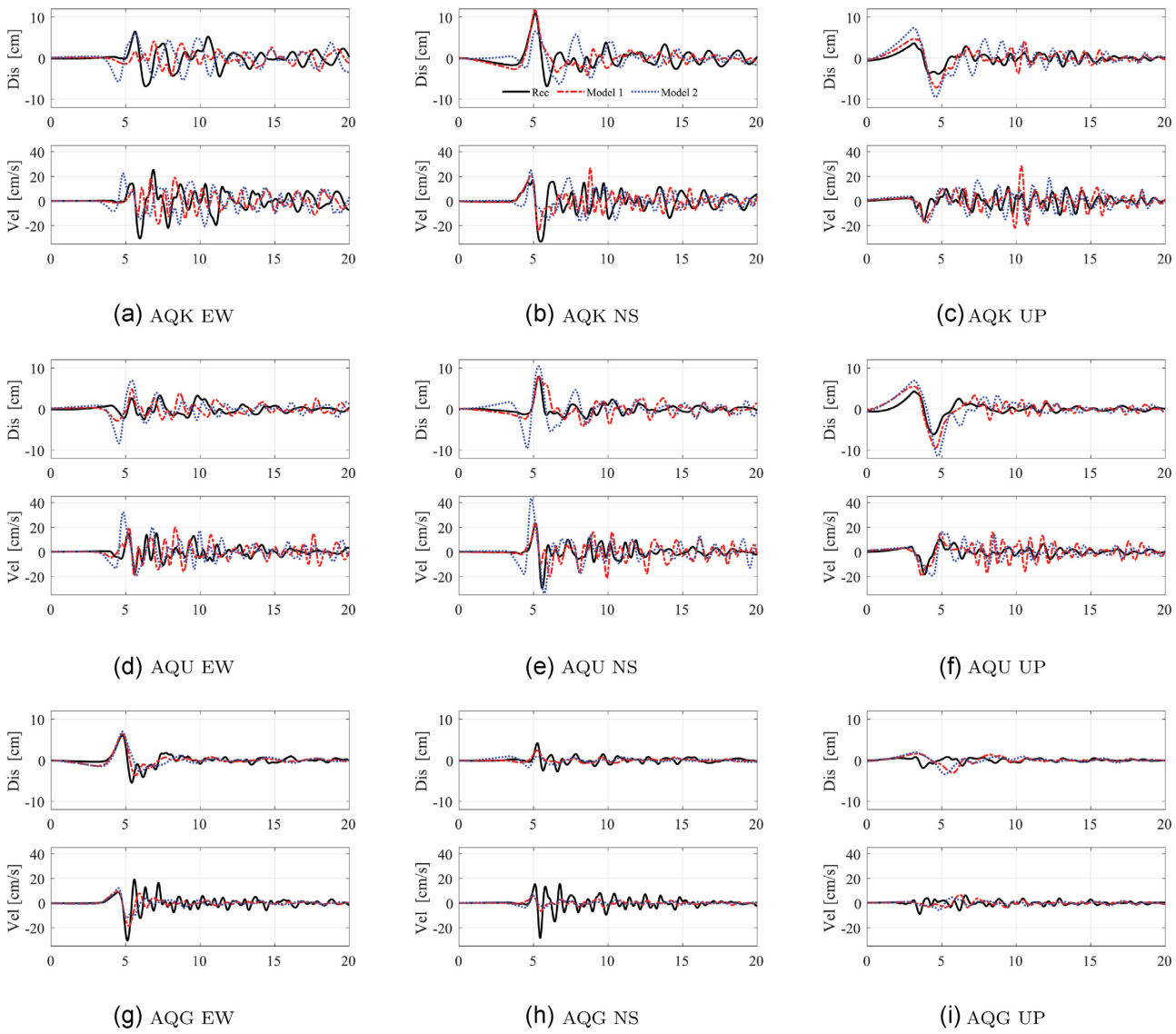

Figure 7. Comparison between the recorded (black lines) and simulated displacement and velocity waveforms for both *Model 1* (red lines) and *Model 2* (blue lines) sources at three stations: AQK, AQU and AQG (see Table 2), in the frequency range [0.1–2.5] Hz.

displacements in the form of slope instabilities, landslides and different erosion processes (e.g. Della Seta *et al.* 2017; Kastelic *et al.* 2017). In the current geodynamic setting, the area is subjected to regional extension of 2–3 mm yr^{-1} (Carafa & Bird 2016; Carafa *et al.* 2020). The effective seismogenic deformation likely represents about 70 per cent of the total regional tectonic extension (Carafa *et al.* 2017) and is expressed also in the form of strong earthquakes, as is the case of 1915 Fucino event, one of the strongest earthquakes ever recorded in the Italian territory (Guidoboni *et al.* 2019; Rovida *et al.* 2019).

The broader L'Aquila area is positioned in the upper and middle Aterno intermountain fluvial basin (UMAB) between the Gran Sasso and Mt Sirente–Mt Cefalone mountain ridges (Fig. 1). Besides the ongoing regional uplift, the zone was subjected to compression expressed along the respective thrust faults that created the high topography terrain and related lower-terrain foredeeps. The activity of younger, leading extensional faults in the UMAB, namely, the SW-dipping Monte Marine-Pettino and Paganica-San Demetrio extensional fault systems (drawn in magenta and red in Fig. 1) further pronounced the topographic difference accentuating the basin depth and simultaneously creating new depositional environment of lacustrine–palustrine to fluvial to alluvial origin.

The UMAB is heterogeneous in its depth and lithological composition. In fact, it is usually described as two distinct basins with NW sector referred to as L'Aquila–Scoppito basin and the SE sector commonly known as the Middle Aterno Valley. The basin itself is interrupted by several intrabasin highs composed of carbonatic or terrigenous bedrock. The UMAB area corresponds to epicentre location of various M_w (or M_e) $\geq$5.5 earthquakes, namely, the 1703 February 2; 1315 December 3; 1461 November 27; 1762 October 6; and 2009 April 6 and 7 earthquakes (Guidoboni *et al.* 2019; Rovida *et al.* 2019) that all caused rather extensive damage through its territory.

We based the reconstruction of the 3-D basin on available data from geological maps (Vezzani *et al.* 1998; Dipartimento Difesa del Suolo 2005a,b,c; Servizio Geologico d'Italia 2010a, b), borehole data (Porreca *et al.* 2016), well logs (Cosentino *et al.* 2017; Nocentini *et al.*

Downloaded from https://academic.oup.com/gji/article/230/1/29/6526874 by INGV user on 22 June 2022

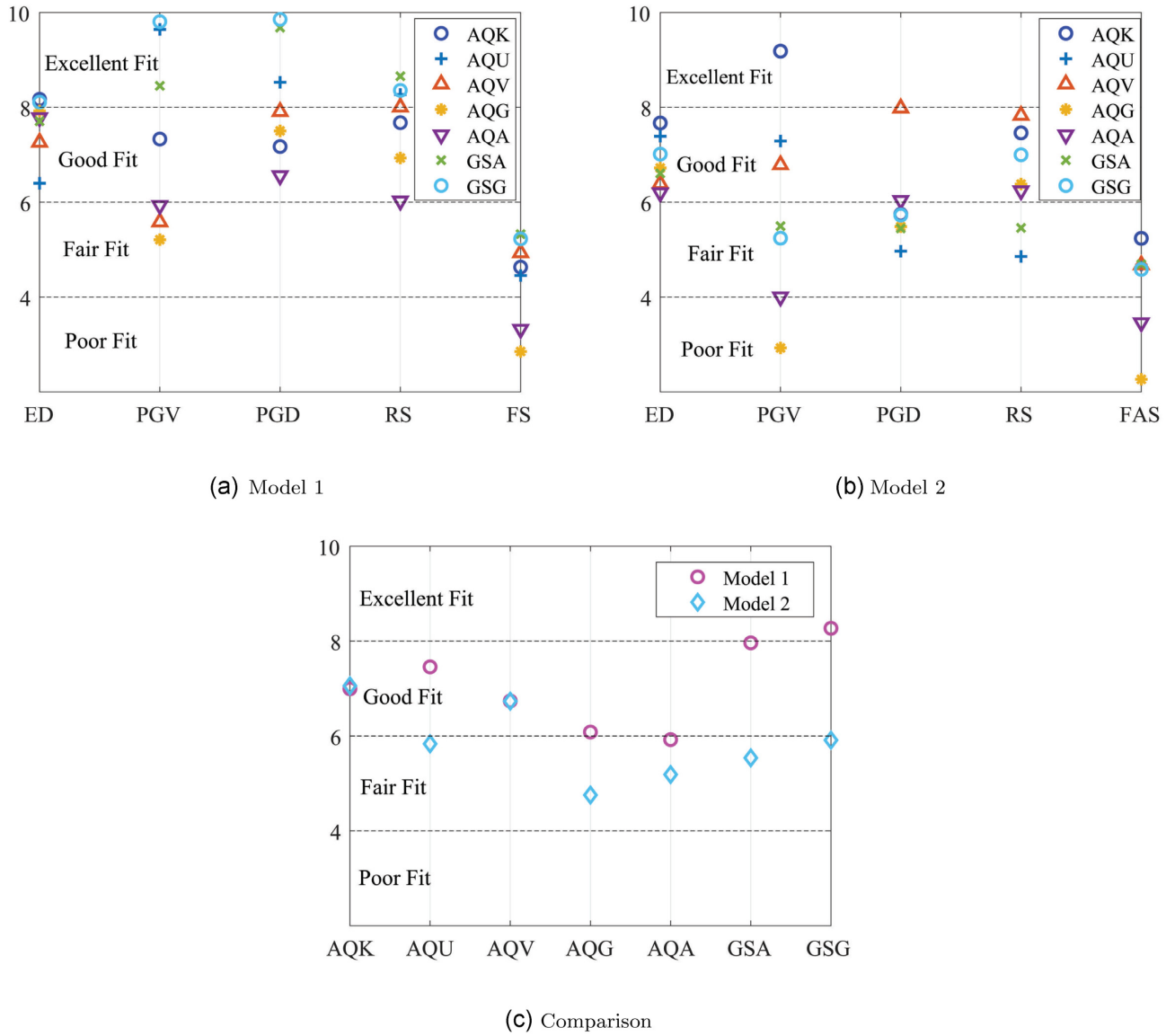

Figure 8. GoF scores at the seven stations listed in Table 2 for the frequency range [0.1–2.5] Hz for each of the five selected parameters. (a) Model 1, (b) Model 2 and (c) the comparison of average scores from the two source models.

2017), seismic profiles (Improta *et al.* 2012; Tallini *et al.* 2012), deep electric resistivity surveys (Balasco *et al.* 2011; Pucci *et al.* 2016) and their interpretations. We further coupled the above-mentioned material with results of microzonation investigation conducted in the broader L'Aquila territory after the 2009 earthquake, the seismic microzonation of the L'Aquila territory project (MS-AQ Working Group and others 2010).

The external borders of the UMAB basin were mapped in order to respect the surface extension of Quaternary lithology, which are the areas where the Quaternary rock or sediment thickness is above zero meters. The spatial extension of the UMAB is from the Campo Imperatore to the N and the Altopiano delle Rocche to the S. We aimed to include in the main basin also the more important fluvial valleys that are influenced by a continuous extension of alluvium, like the Valle del Salto at the basin W extension.

Besides the basin extension limit where the Quaternary infill thickness is set to zero, we, based on the retrieved data, mapped further six isolines corresponding to 30, 115, 225, 400, 480 and 640 red metres Quaternary infill thickness. These values were chosen based on the geometry of the basin along the sections with the best data coverage, considering the overall distribution of the basin infill thickness. Starting from the points with known infill thickness we can interpolate the parameter values for the entire basin extension through a triangulation approach. The SE UMAB sector is larger and deeper with respect to its NW counterpart. The greatest infill thickness of 640 m is reached in the San Demetrio area, the portion of the UMAB with greatest gradients in the basin geometry. The local high in the basin geometry separates the deepest basin section from its NW continuation, where infill thickness reaches 400 m. Local depocentres where infill thickness reaches or surpasses 400 m of smaller dimensions are present also in the central part of the UMAB. The SE sector is composed of three different systems (Giaccio *et al.* 2012; Nocentini *et al.* 2018), while in the NW sector two different depositional events were recognized (Mancini *et al.*

Downloaded from https://academic.oup.com/gji/article/230/1/29/6526874 by INGV user on 22 June 2022

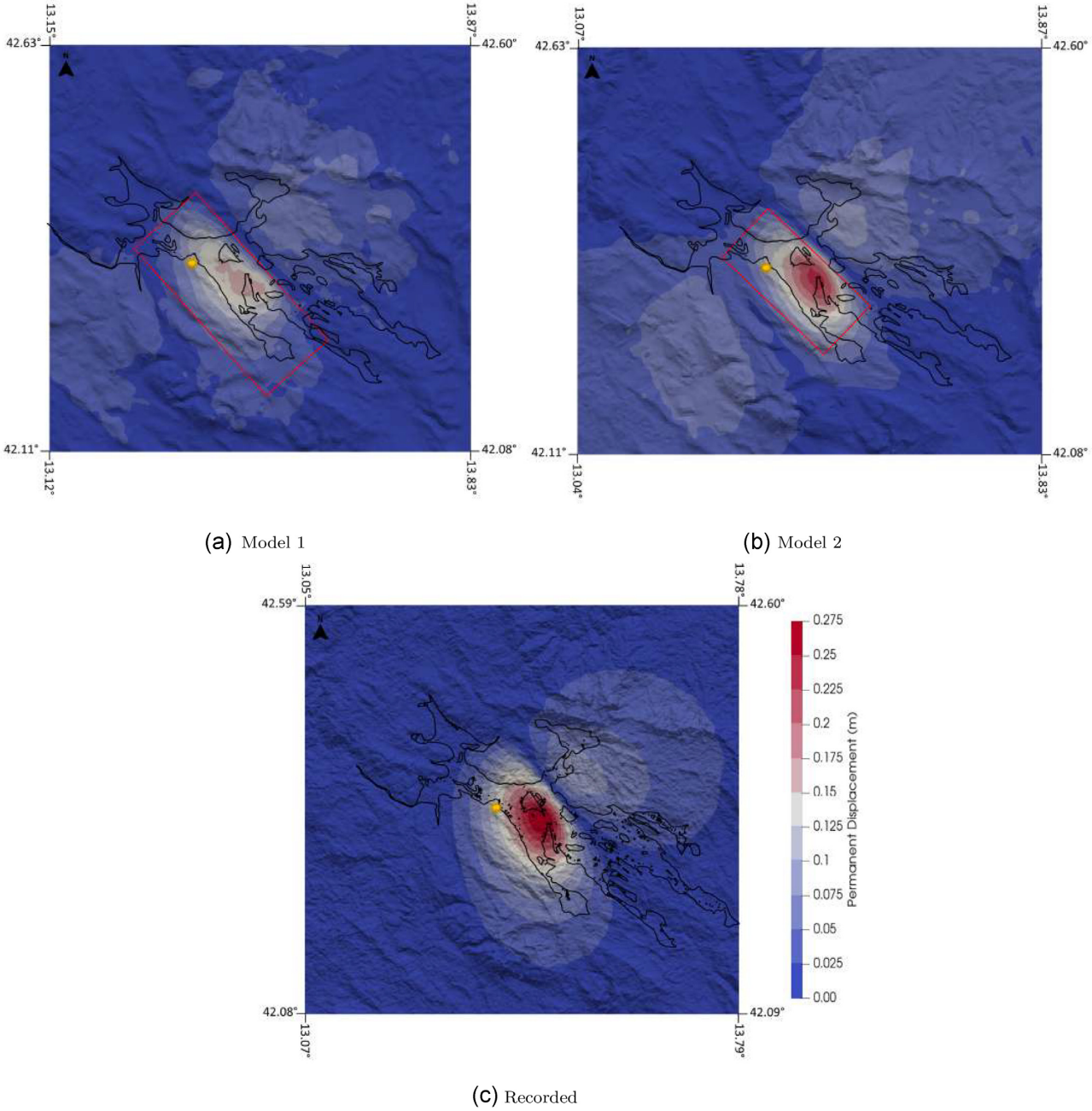

Figure 9. Modulus of the permanent displacement registered at 30 s for source *Model 1* (a) and *Model 2* (b), compared to the co-seismic displacement obtained by satellite data (c) (courtesy of Simone Atzori).

2012). The first basin infill consists of talus breccias and slope-derived breccias, debris-flow deposits and alluvial clayey-sandy conglomerates (Bertini & Bosi 1993; Cosentino *et al.* 2017). The laYes custrine sedimentary units, mainly composed of calcareous silts, clays, lignite and occasionally also tephra layers (Bosi & Bertini 1970; Centamore *et al.* 2010; Nocentini *et al.* 2018), are recognized in the deeper basin sectors. Laterally, the lacustrine units pass to heterogeneous delta type sedimentation of coarser grained units. During its evolution the depositional environment passed to more palustrine sedimentation type environment influenced also by local erosion that caused the presence of coarser sandy to conglomeratic material in between a finer grained silts (Macrì *et al.* 2016). Progressively the environment passed to prevailing fluvial-alluvial derived mid to coarse grained sedimentation type, many times organized in the form of fluvial terraces (e.g. Nocentini *et al.* 2018). The youngest basin infill is represented by the Holocene fluvial, colluvial, scree deposits and landslides (e.g. Dipartimento Difesa del Suolo 2005a; Centamore *et al.* 2010) related to the erosional and depositional processes still active in the UMAB basin.

The detailed basin reconstruction was designed with the scope of improving our knowledge on the basin subsurface characteristics, keeping in mind that wave propagation and local ground motion amplification are controlled mainly by geometric complexities in the buried bedrock topography and seismostratigraphic properties of the sedimentary infill (Bard & Bouchon 1980; De Luca *et al.* 2005).

Downloaded from https://academic.oup.com/gji/article/230/1/29/6526874 by INGV user on 22 June 2022

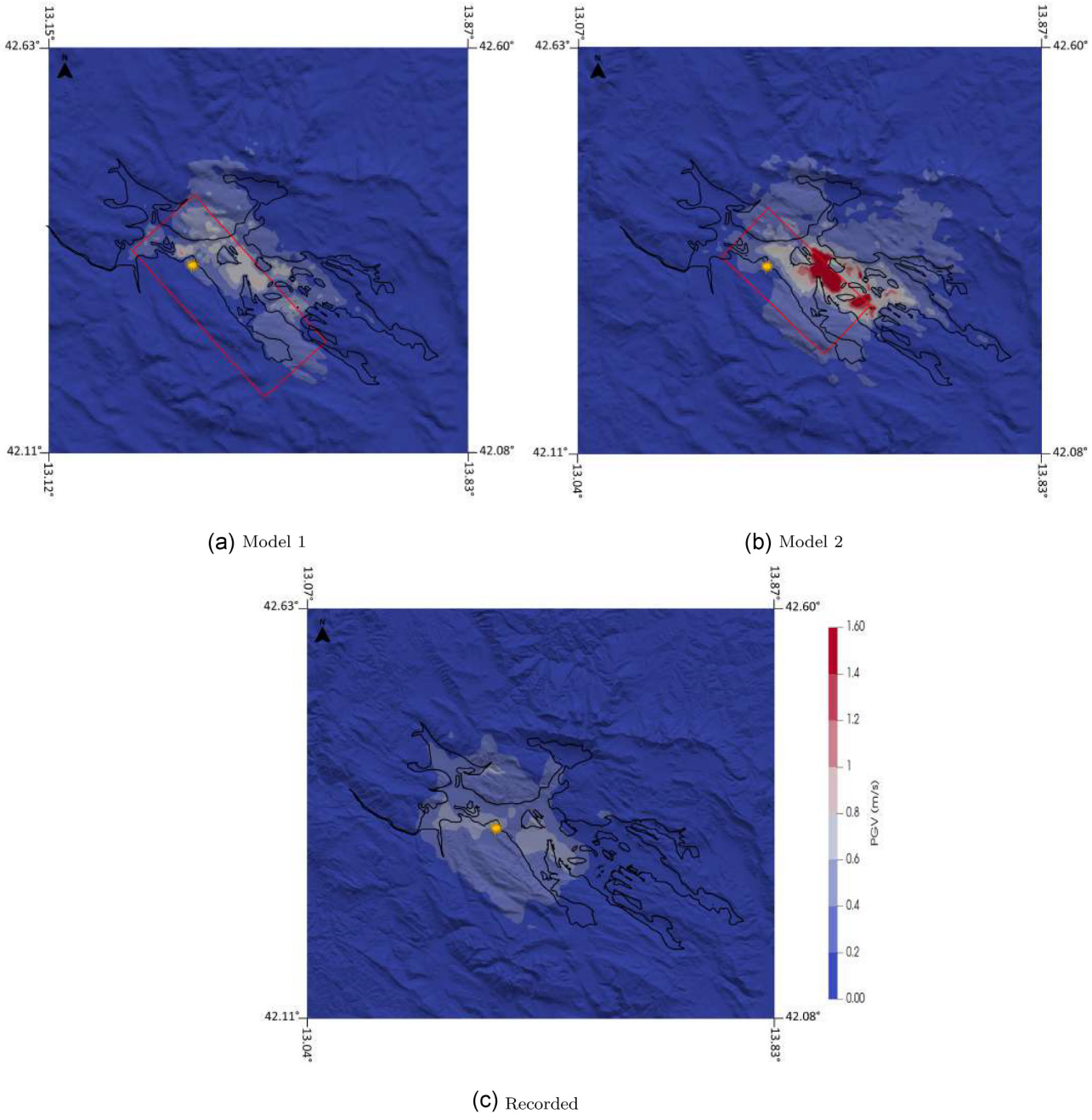

Figure 10. Comparison between PGV maps obtained from simulation *Model 1* (a) and *Model 2* (b), panel (c) shows the recorded data from shakemaps.

A homogeneous linear visco-elastic seismo-stratigraphic profile has been assumed for the alluvial deposits inside the Aterno Valley, according to Evangelista *et al.* (2017):

$$V_S = 300 + 36 \cdot z^{0.43} (\mathrm{m\,s^{-1}}),\ V_P = V_S\sqrt{4.57},\ Q_S = 0.10 V_S,\ \rho = 1.9\,(\mathrm{g\,cm^{-3}}). \quad (1)$$

where z denotes the depth from the topographic surface, V_S is the shear wave velocity, V_P is the compressional wave velocity, ρ is the soil mass density and Q_S is the S-wave quality factor defined from the V_S profile. Outside the Aterno Valley, a horizontally layered crustal model is assumed as in Table 1 (see Ameri *et al.* 2012; Evangelista *et al.* 2017, and references therein for more details)

Downloaded from https://academic.oup.com/gji/article/230/1/29/6526874 by INGV user on 22 June 2022

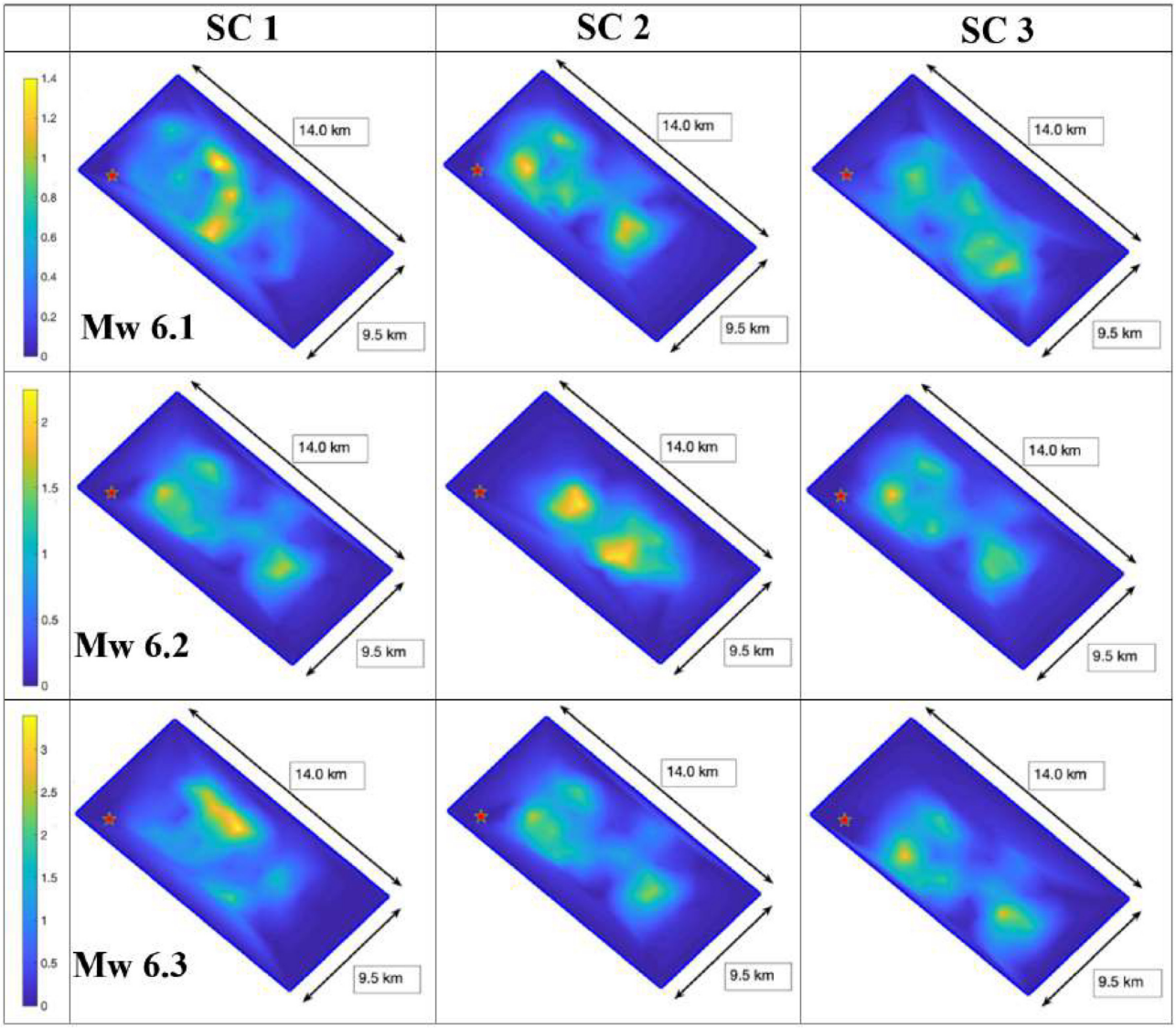

Figure 11. Slip distributions obtained using the rupture generator model developed in Schmedes *et al.* (2013).

2.2 Automated domain reconstruction software

In this work, a high-resolution topography was considered during the generation of the computational grid. The importance of having an optimal topography representation for physics-based numerical simulations has been considered several times, we refer, for example, to Lovati *et al.* (2011); Hailemikael *et al.* (2016); Asimaki & Mohammadi (2018) and references therein.

Different reconstruction techniques have been employed to define the Earth surface starting from georeferenced data. Depending on the area of interest and on the level of accuracy required, a surface reconstruction may take anything from minutes to days to create, requiring constant human inputs. Moreover, careful selection of the programming language used is required in order to provide outputs compatible with the software employed for the mesh generation: in our case Coreform Cubit (`https://coreform.com/products/coreform-cubit`).

In order to simplify the construction of an accurate Earth's surface as well as a 3-D computational domain in a quick and simple way, while requiring minimal input, we have designed a set of Python (`https://www.python.org/`) scripts that interface directly with Coreform Cubit. These scripts allow for the creation of: (i) a topographical surface of any size; (ii) a cake-layered 3-D domain; (iii) a given number of fault planes to be included in the model, *cf.* Fig. 2.

The scripts require users' inputs at the initial step and then proceed to generate the domain in an automatic way. This allows the creation of several distinct domains in a simple, time effective manner in parallel.

An overview of the workflow we have designed to build a computational model in Coreform Cubit is summarized in Fig. 2. A more detailed explanation, as well as timing examples, can be found in May *et al.* (2021).

Downloaded from https://academic.oup.com/gji/article/230/1/29/6526874 by INGV user on 22 June 2022

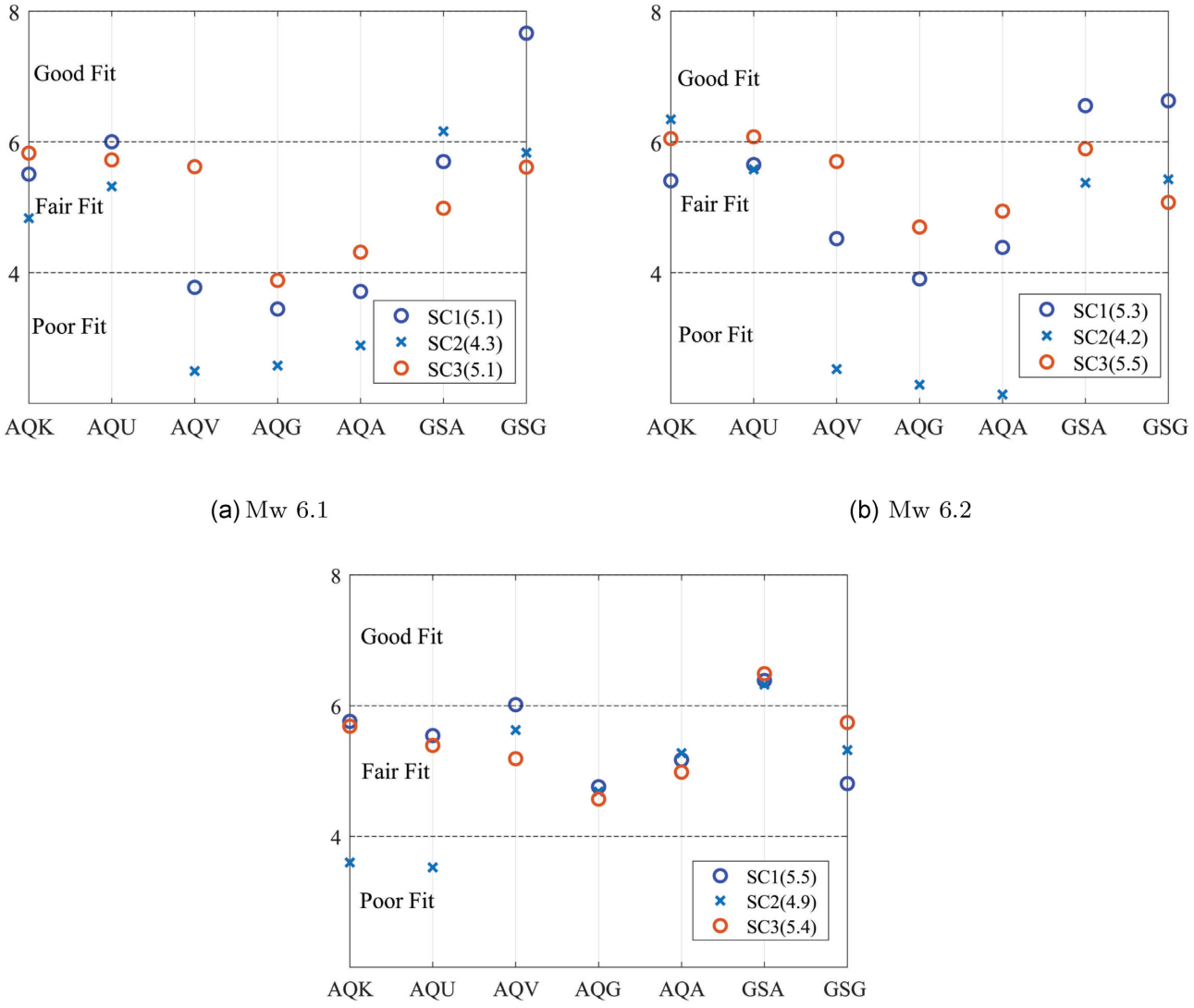

Figure 12. Average GoF value of the five metrics for all the stations under consideration for the scenario with M_w 6.1 (a), M_w 6.2 (b) and M_w 6.3 (c) in the frequency range [0.1,2.5] Hz.

3 PARAMETRIC STUDY ON THE KINEMATIC SEISMIC SOURCE

In the previous section, we outlined the procedure used to obtain a detailed reconstruction of the geomorphological structure of the study area (basin and topography). However, a well-constrained model for a seismic source is crucial to obtain accurate results, especially in the near-source region where ground motion features are governed by the details of the fault rupture process. Within this paper the seismic source is represented by a kinematic model on a prescribed fault defined geometrically by a plane, approximating the real fault structure.

The aim of this subsection is to compare the numerical results obtained by using two kinematic sources, retrieved from the finite-fault solutions available from literature studies for the M_w 6.3 2009 April 6 earthquake. The sources are obtained using two different techniques, one from the inversion of the recorded ground motions and the second one employing the DInSAR technique. This choice has been done with the aim of comparing the impact of the two approaches for source inversion on the results of physics-based 3-D simulation. Note that, for each kinematic source, a 3-D mesh has been constructed that matches exactly the geometry of the fault plane. The kinematic source models adopted as well as the computational domains considered are provided in Figs 3 and 4, respectively.

All simulations discussed in this work are done using the code SPEED. In this numerical tool, the viscous elastodynamic equation, describing the soil displacement, is approximated using the discontinuous spectral element method in space coupled with the leap-frog scheme in time. SPEED allows one to use non-conforming meshes and different polynomial approximation degrees in the numerical model. This makes mesh design more flexible (since grid elements need not match across interfaces) and permits the selection of the best-fitting discretization parameters in the computational domain, while controlling the overall accuracy of the approximation. More specifically, the

Downloaded from https://academic.oup.com/gji/article/230/1/29/6526874 by INGV user on 22 June 2022

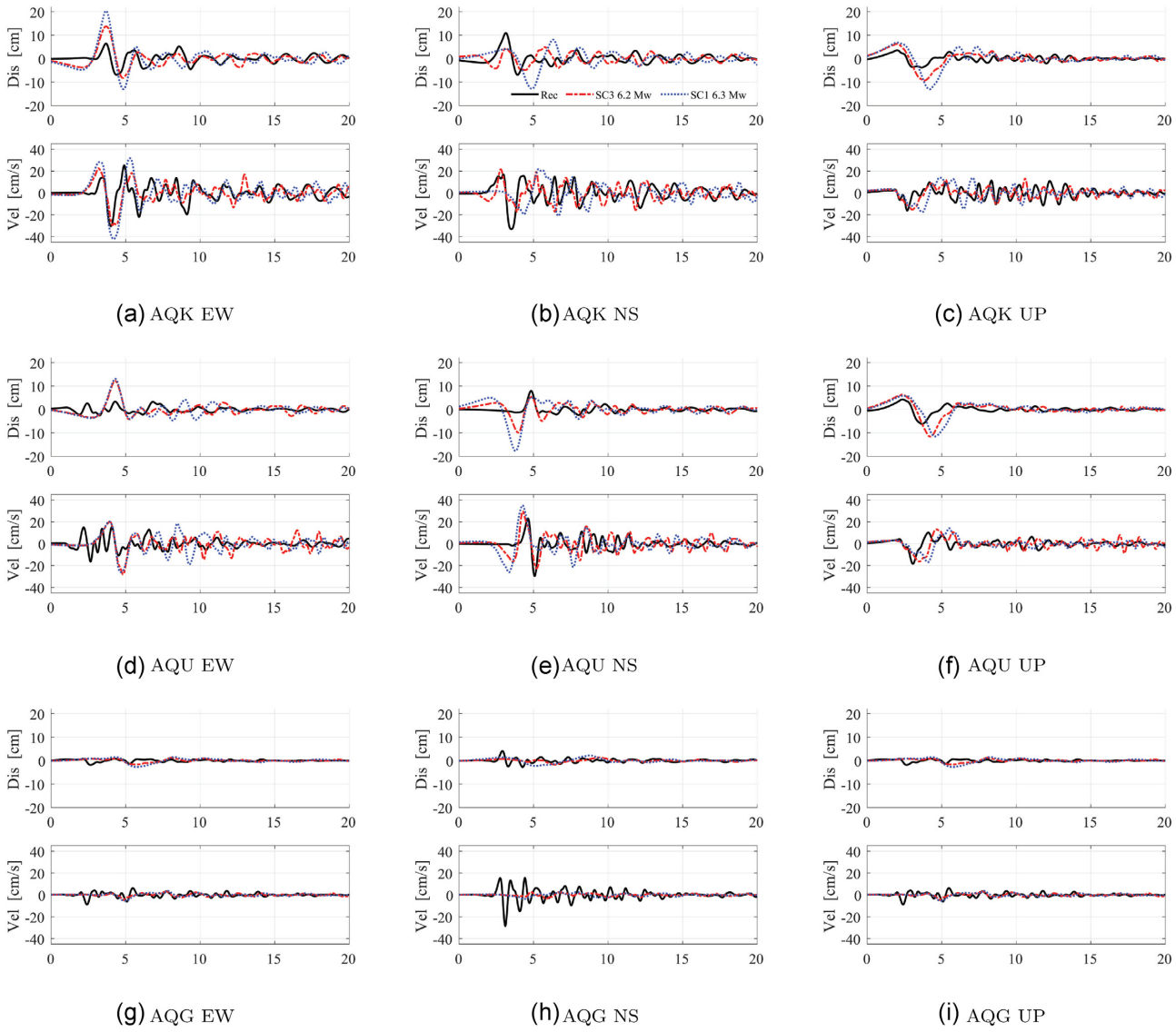

Figure 13. Comparison between recorded (black lines) and simulated waveforms for the stations AQK, AQU and AQG, in the frequency range [0.1, 2.5] Hz for scenarios M_w6.2-SC3 (red lines) and M_w6.3-SC1 (blue lines).

numerical mesh may consist of smaller elements and low-order polynomials where wave speeds are slowest, and of larger elements and high-order polynomial where wave speeds are fastest. We refer the reader to Antonietti *et al.* (2012, 2016) and Ferroni *et al.* (2017) for the analysis of the scheme; to Mazzieri *et al.* (2013) for implementation details; and to Smerzini & Villani (2012), Paolucci *et al.* (2015, 2016), Infantino *et al.* (2020) and Paolucci *et al.* (2021a) for other relevant applications in computational seismology.

The first source, constructed by Ameri *et al.* (2012), has been obtained by inverting strong ground motion data and it has previously been used in Evangelista *et al.* (2017) on a different 3-D computational model. Details about the kinematic source and fault geometry can be found in Figs 3 (left) and 4(a), respectively. Rise time and rupture velocity are randomly distributed around mean values of 0.7 s and 2500 m s^{-1}, respectively.

The second kinematic source has been provided from Atzori *et al.* (2009) and it has been derived by DInSAR technique using the images of permanent displacement provided by ENVISAT and COSMO−SkyMed satellites. The slip values, assigned on the fault plane, are not constant and reach a maximum value of approximately 90 cm (see Fig. 3, right). The geometric parameters of the fault are summarized in Fig. 4(b). Rise time and rupture velocity distribution are assumed to be constant, that is 0.7 s and 2500 m s^{-1}, respectively. Hereafter, the *Ameri et al.* and *Atzori et al.* source models are referred to as *Model 1* and *Model 2*, respectively.

Many other slip distributions are available in literature. See, for example Cheloni *et al.* (2010), Avallone *et al.* (2011), Yano *et al.* (2014) and references therein.

The grids considered for *Model 1* and *Model 2* have approximately 8×10^5 and 40×10^5 nodes, respectively. Both meshes are able to propagate frequencies up to approximately 2.5 Hz, *cf.* Fig. 4.The simulation of *Model 1* took approximately 14 hr walltime, with time step 0.0005 s and final time $T = 30$ s, on two nodes consisting of DELL R730 2 CPUs Intel Xeon E5-2698 2.20GHz, RAM 256Gb using (18022a

Downloaded from https://academic.oup.com/gji/article/230/1/29/6526874 by INGV user on 22 June 2022

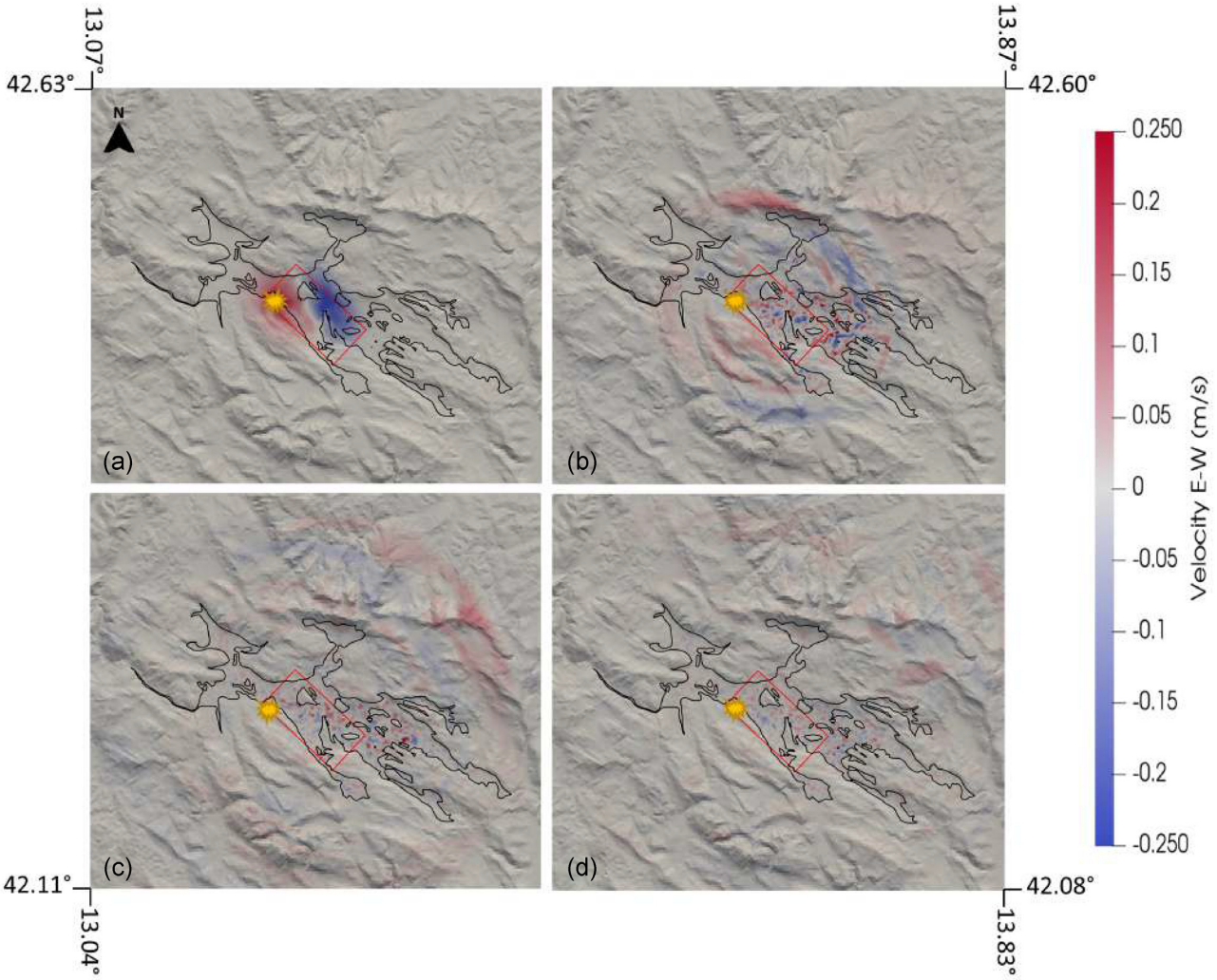

Figure 14. Snapshots of the velocity field in the E–W direction for scenario M_w 6.2-SC3 at times 3.5 s (a), 7.5 s (b), 13.5 s (c) and 17.5 s (d).

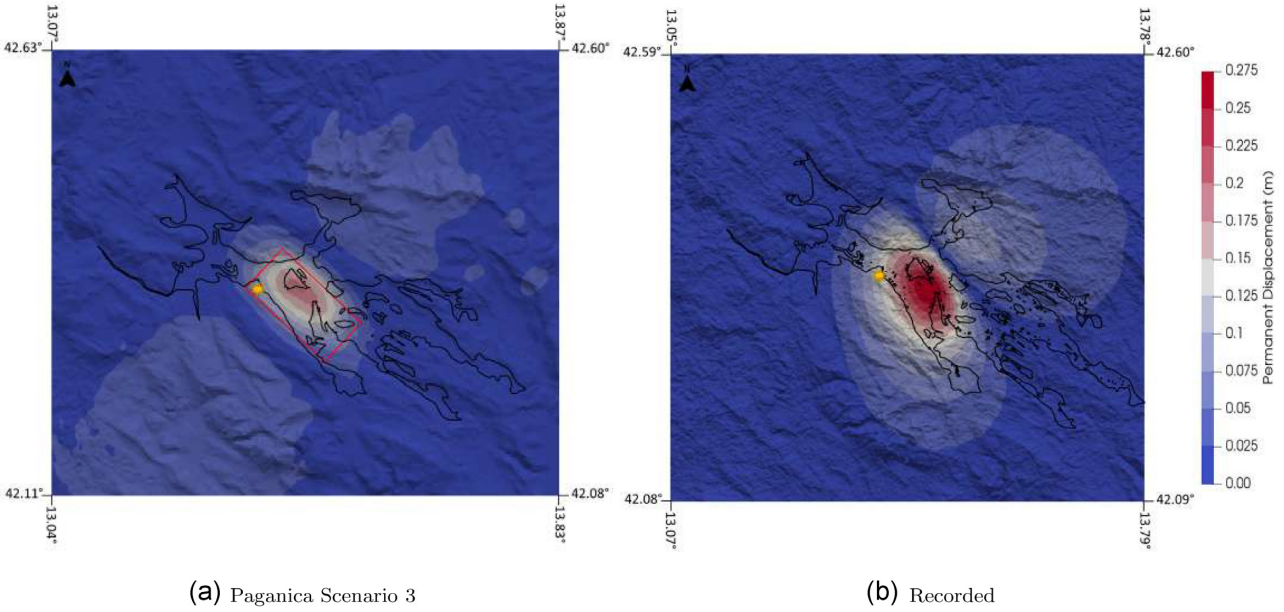

Figure 15. Permanent displacement registered after 30 s for the third scenario 6.2 M_w (a) compared to the co-seismic displacement obtained by satellite data (b) (courtesy of Simone Atzori).

Downloaded from https://academic.oup.com/gji/article/230/1/29/6526874 by INGV user on 22 June 2022

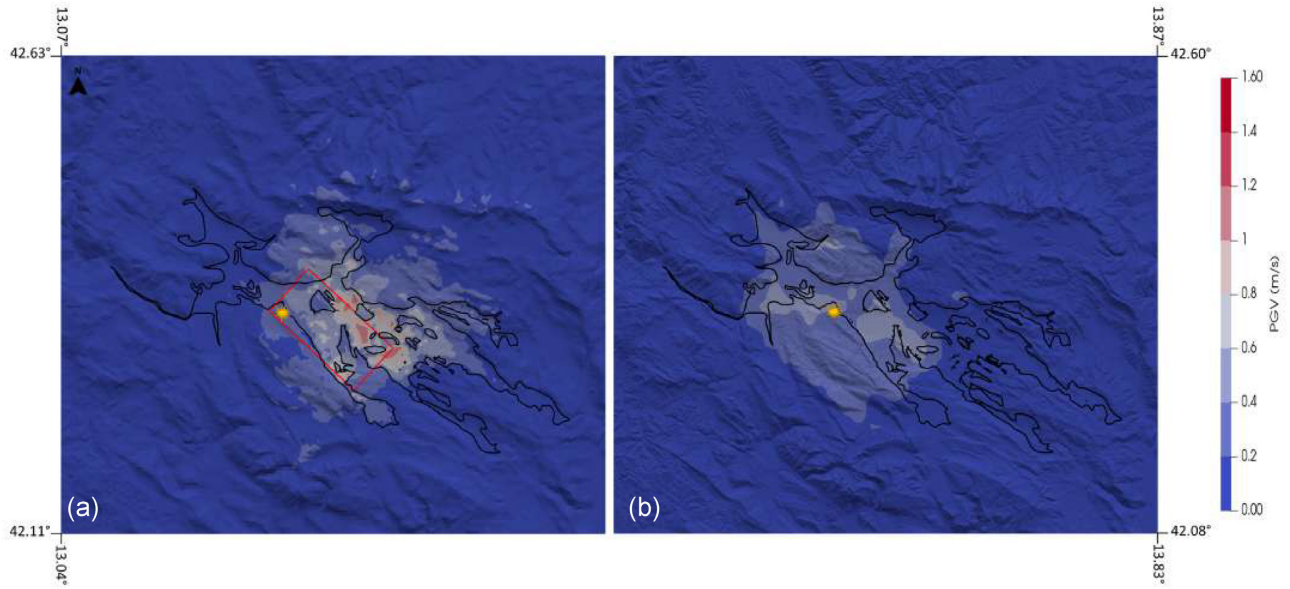

Figure 16. Comparison between simulated (a) PGV map (M_w6.2-SC3) and ShakeMap (b) from http://shakemap.ingv.it/shake/archive/.

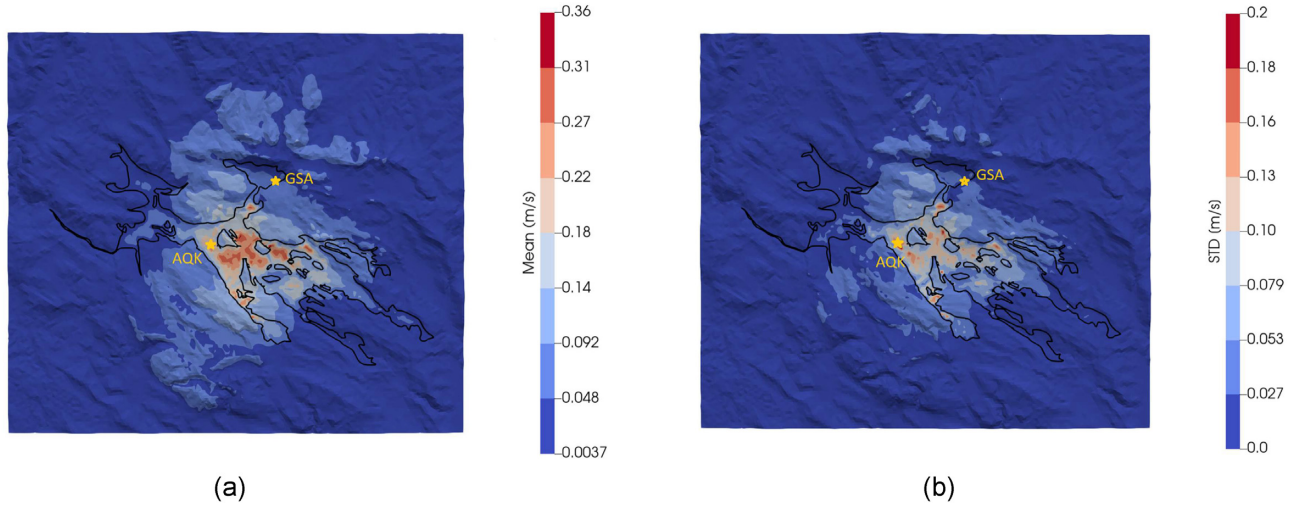

Figure 17. Mean value (a) and standard deviation (b) of the PGV, N–S component, across the nine scenarios.

MPI-threads) installed on Caliban Cluster (https://caliband.disim.univaq.it). *Model 2* simulations took 60 hr walltime, with time step 0.00025 s and final time $T = 30$ s, on one node containing HP Proliant DL 580 Gen 10 with 4 CPUs Intel Xeon Gold 6140M 2.30GHz, RAM 512Gb using (140 MPI-threads) on Caliban Cluster.To validate the computational models, we compare our results with the available near-source recordings located within 20 km of epicentral distance, see Table 2.

In Figs 5 and 6, snapshots of the horizontal (E–W) velocity wavefield simulated by SPEED at four different times are shown for the *Model 1* and the *Model 2*, respectively. In the first panel, we can observe the initiation of the rupture, consistently with the assumed focal mechanism (normal), whereas in the subsequent panels the trapping of seismic waves inside the basin is apparent. In Fig. 7, the time histories of displacement and velocity waveforms simulated at three stations, namely, AQK, AQU and AQG (see Table 2) are shown and compared with the recorded ones, for the three components of motion [E–W, N–S and up–down (UD)].

The agreement between recorded and simulated waveforms is rather satisfactory, both for the displacement and the velocity field, especially at the stations AQK and AQU, with good fit in terms of first arrivals, predominant frequencies and peak values. A poor agreement is found at AQG station, in particular for the NS component, with underestimation of simulations, most likely because of the lack of some asperities in the slip distribution across the fault towards the NW sector of the Aterno Valley as well as the simplified velocity model assumptions.

To have a quantitative evaluation of the performance of the numerical model, the goodness-of-fit (GoF) criteria introduced by Anderson (2004) are evaluated. We recall that for each parameter a goodness-fit score ranging from 0 to 10 is assigned: 'poor fit' is obtained for values smaller then 4, 'fair fit' between 4 and 6, 'good fit' between 6 and 8, and 'excellent fit' between 8 and 10. Here, the GoF is computed considering five parameters, including integral, peak and spectral measures, regarded as the most significant from an engineering point of

Downloaded from https://academic.oup.com/gji/article/230/1/29/6526874 by INGV user on 22 June 2022

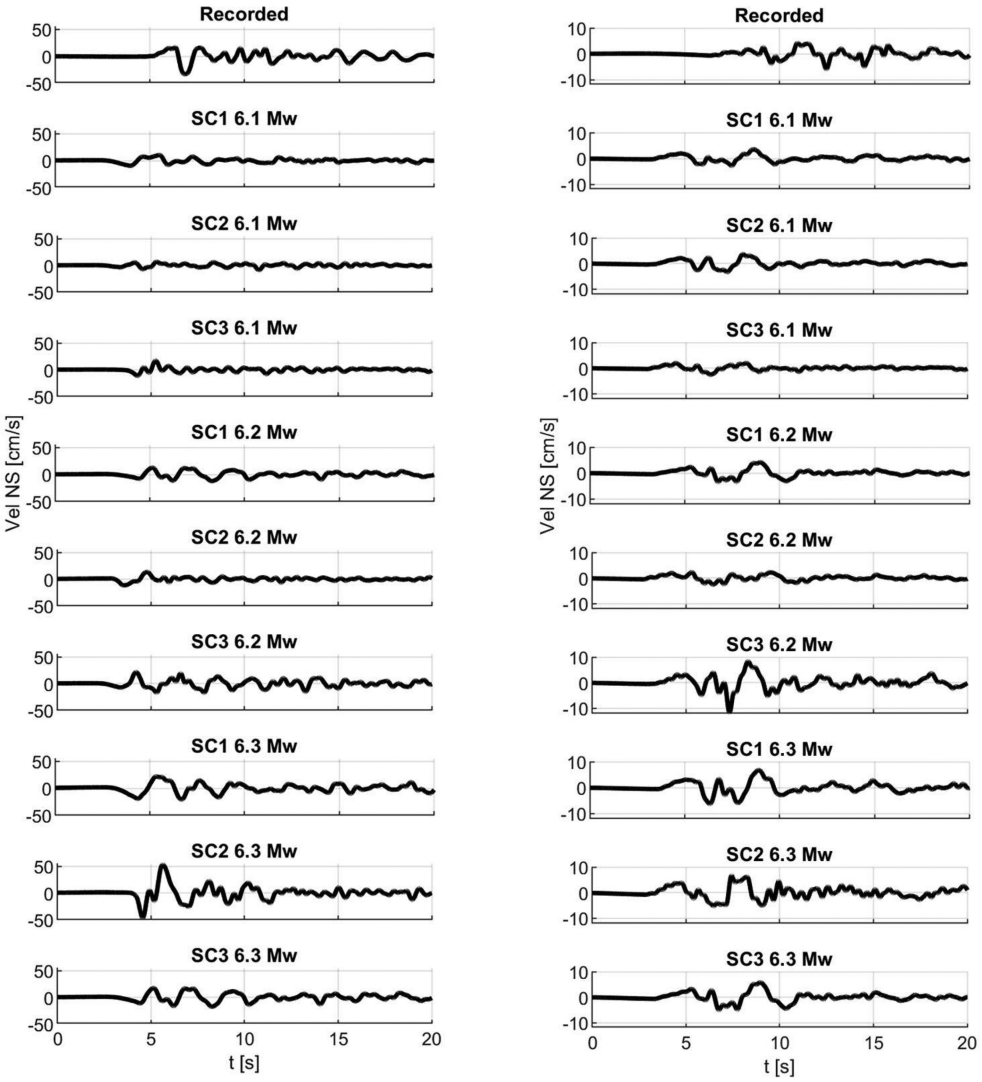

Figure 18. Comparison between the N–S velocity component of recorded signal and of the nine simulated scenarios. Two receivers are considered, namely, AQK (a) and GSA (b), corresponding to a high and a low value of standard deviation, respectively (see Fig. 17b).

view, namely, *energy duration* (ED), *peak ground velocity* (PGV), *peak ground displacement* (PGD), *response spectral acceleration* (RSA) and *Fourier amplitude spectra* (FAS).

In the following, the simulated and recorded data will be referred to as subscripts 's' and 'r', respectively. We define

$$I_{\mathrm{E}}(t) = \int_0^t v(s)\mathrm{d}s, \tag{2}$$

$$\mathrm{ED} = 10\left[1 - \max\left(\left|\frac{I_{\mathrm{E_r}}(t)}{I_{\mathrm{E_r}}(T)} - \frac{I_{\mathrm{E_s}}(t)}{I_{\mathrm{E_s}}(T)}\right|\right)\right]. \tag{3}$$

$$\mathrm{PGV} = S(|\max(v_{\mathrm{r}}(t) - \max(v_{\mathrm{s}}(t)|), \ \mathrm{PGD} = S(|\max(d_{\mathrm{r}}(t) - \max(d_{\mathrm{s}}(t)|). \tag{4}$$

$$\mathrm{RAS} = \mathrm{mean}(S(\mathrm{RAS_r}(f) - \mathrm{RAS_s}(f)), \ \mathrm{FAS} = \mathrm{mean}(S(\mathrm{FAS_r}(f) - \mathrm{FAS_s}(f)). \tag{5}$$

Fig. 8 shows the GoF scores obtained at the seven stations listed in Table 2 for the five aforementioned parameters, for both *Model 1* and *Model 2* source models (Figs 8a and b, respectively). For each station, the symbol shown indicates the average value obtained from the three components. Moreover, in Fig. 8(c), we report the scores obtained by averaging the five parameters with respect to each station. It turns out that the GoF is higher for *Model 1* than for *Model 2*, at least in the considered range of frequencies. In particular, we underline

Downloaded from https://academic.oup.com/gji/article/230/1/29/6526874 by INGV user on 22 June 2022

that for *Model 1* the average value of the five parameters is in the 'good fit' range for all the stations considered, except AQA, for which the GoF score is slightly less than the 'good fit' threshold, that is 6.0. Comparing these results with the ones present in literature, for example Smerzini & Villani (2012) and Evangelista *et al.* (2017), we note an improvement of the overall GoF scores. Furthermore, from Figs 8(a) and (b), we can see that for both sources the scores associated with the ED parameter are between 6 (good) and 8 (excellent) for all stations, with limited dispersion. This suggests a good agreement between the recorded and simulated velocities, *cf.* Fig. 7. As a further validation, in Fig. 9 the modulus of the permanent displacement vector at the time instant = 30 s for both *Model 1* (a) and *Model 2* (b) is compared to the co-seismic displacement obtained by geodetic measurements (c) (courtesy of Simone Atzori, INGV). For both sources the largest displacement, of around 17.5 cm for *Model 1* and 25 cm for *Model 2*, is reached on the hanging wall of the fault, a few kilometres SE of the epicentre. The source *Model 1* underestimates, by around 40 per cent, the satellite deformation field, which is better described by *Model 2*, where maximum underpredictions of approximately 15 per cent are found. This is expected since *Model 2* is based directly on the inversion of DInSAR data. These misfits can be attributed to the assumptions at the base of the kinematic source model, such as the regular, smooth geometry of the fault and the simplified 1-D visco-elastic soil model considered for the inversion.

Finally, in Fig. 10, we compare the PGV maps, obtained from our numerical simulations with the one provided in http://shakemap.ingv.it/shake/archive/. In our framework, the PGV maps contain the maximum between the E–W and N–S components of the velocity. Note that the resolution of our model is around 2–2.5 Hz and PGV is typically associated with frequencies below this limit (see Paolucci & Smerzini 2018), therefore the comparison with ShakeMaps can be expected, at first approximation, to show a reasonable good agreement. On the one hand *Model 1* reproduces quite well the measured PGV map. On the other hand *Model 2* tends to provide higher maximum PGV values.

4 'BLIND PREDICTION' TEST

In the previous section, we have shown a quantitative comparison between numerical simulations and recorded data of the M_w 6.3 2009 April 6 L'Aquila earthquake. The former have been obtained using a detailed information about the seismic source, as well as detailed geophysical reconstruction of the Aterno Valley. In this section, we try to simulate the main event using basic information typically available a few minutes after the earthquake (magnitude, epicentre location and fault geometry). In other words, we made a kind of blind prediction exercise to explore to which extent the simulated scenario agrees with the observed ground motions, when little *a-priori* information on the event is available.

For this purpose, as basic input data, we considered: (i) the Paganica fault geometry, as provided in DISS (http://diss.rm.ingv.it/dissGM/); (ii) the epicentre location at 42.34 Lat–13.38 Long with depth fixed at 9 km (value considered reasonable for seismic events occurring on the central Apennines having approximately M_w 6); and (iii) a magnitude M_w range from 6.1 to 6.3 to account for the typical uncertainty in magnitude estimation. Regarding the causative fault (i), it is worth recalling that the Paganica fault was not included in the DISS database prior to the L'Aquila earthquake. The Paganica fault extends for 14 km in length and 9.5 km in width; strike, dip and rake are 133°, 43° and 275°, respectively.

The details of the 3-D computational domain adopted for these earthquake scenarios are summarized in Fig. 4, on the third row. For each scenario earthquake associated with a prescribed magnitude level, we considered three different source rupture realizations, leading to a total of nine simulations. The fault rupture realizations are generated using the kinematic model generated by Schmedes *et al.* (2013). Fig. 11 illustrates the nine slip distributions considered for these scenarios. Note that each scenario is identified by a fault rupture plane and by a magnitude value, while a rupture realization refers to a particular slip distribution (and corresponding parameters, such as rupture time and rise time) on the given fault plane.

Starting from the nine ground motion simulations, we computed the GoF scores by averaging the five metrics considered previously, that is ED, PGV, PGD, RS and FAS, for the three different components of the considered field. Fig. 12 shows the score as a function of the considered earthquake scenario for M_w 6.1 (Fig. 12a), M_w 6.2 (Fig. 12b) and M_w 6.3 (Fig. 12c) and rupture realization (referred to as SC1, SC2 and SC3, for each magnitude).

As one can see, the scenarios that produced the best average GoF score, of around 5.5, are the scenarios M_w6.2-SC3 and M_w6.3-SC1. For these two scenarios, in Fig. 13, the comparison between the three-component recorded and simulated waveforms are shown at AQK, AQU and AQG stations. In each of the three scenarios, the stations AQV, AQG and AQA produce relatively low fit scores; this is likely due to an incomplete geological description of that region. To improve the result in this sense, a lower scale model is needed. Note that, in each of the three scenarios, the stations AQV, AQG and AQA produce relatively low fit scores, most likely due to a combined effect of the source model, radiating limited energy in the west direction regardless of the adopted slip distribution, and of deficiencies in the local site response model.

In general, the agreement is satisfactory, in particular for the stations closest to the epicentre (AQK and AQU) for both scenarios. At AQG, the displacement time history is quite well reproduced in the EW and UD components especially in terms of peak values. The velocity, however, is strongly underestimated except for the UP direction. These misfits turn out to be stronger than the ones observed for the source models specifically calibrated on the L'Aquila observations, namely *Model 1* and *Model 2*. This suggests that the source, rather than approximations in the domain reconstruction, plays a major role in this analysis. Finally, we further analyse the M_w6.2-SC3 scenario, as it seems to reproduce more effectively the observed data at AQK and AQU stations.

Downloaded from https://academic.oup.com/gji/article/230/1/29/6526874 by INGV user on 22 June 2022

The considered source is able to reproduce the up-dip rupture mechanism in a satisfactory way (see Fig. 14), but, as shown in Fig. 15, the observed co-seismic displacement is strongly underestimated, likely due to assumptions of the random source. A better result could be obtained by a wider set of earthquake scenarios and by considering the average value of the computed co-seismic displacement. This, however, is beyond the scope of this work.

Finally, we compare the simulated PGV map from scenario M_w6.2-SC3 with the ShakeMaps for the L'Aquila main shock provided at http://shakemap.ingv.it/shake/archive/ (see Fig. 16). Although there is a general agreement between the two maps, it is quite clear that the simulated ground shaking map includes a small-scale spatial variability that cannot be reproduced by the ShakeMap approach. Such a variability is related to the details of the alluvial basin coupled with those of the fault rupture process. It is noted that in the simulated map higher PGV values are obtained, especially in the SE direction, likely owing to the interaction of source directivity with the response of the basin where the sediments are of considerable thickness (see Fig. 1).

Although the number of simulations is not sufficient for a robust statistical analysis, Fig. 17 shows the mean and the standard deviation of the PGV, N–S component, calculated considering all scenarios. As expected, higher values of standard deviation can be found within the deeper part of the basin on the surface projection of the causative fault, where the effects of the extended source couple with those of complex (3-D) local site amplification. In this region, the value of the standard deviation reaches 20 cm s^{-1} in some localized areas. This observation is confirmed by looking at the time histories recorded at AQK (see Fig. 18a). As a matter of fact, the nine scenarios show a different trend from each other, and also with respect to the recorded signal. A lower variability is observed instead in correspondence of seismic station GSA (Fig. 18b), located on outcropping bedrock and farther from the source.

5 CONCLUSIONS AND FUTURE WORKS

In this paper, we simulated the 2009 April 6 L'Aquila earthquake using the numerical library SPEED. Our results show the importance of a well-constrained kinematic source model for near-source ground motion prediction. From this study, it turns out that the best-fitting source model is the one proposed in Ameri *et al.* (2012) (*Model 1*), in agreement with previous studies on 3-D physics-based simulations of L'Aquila earthquake. Besides the source model, we also show that a careful and detailed reconstruction of the geology and morphology of the area appears decisive for the accuracy of the obtained results. The results of this study are in satisfactory agreement with the observed ground motion features, especially for *Model 1*, where the average GoF is contained in the good fit region (*cf.* Fig. 8c). Moreover, performing a blind prediction test, we show that it is possible to simulate an earthquake with acceptable accuracy, with a minimal set of input data on the target seismic event. The sensitivity of the prediction capability of simulated ground shaking scenarios with respect to the uncertainty of selected source parameters (such as the slip distribution) is a key aspect in ground motion prediction and it will be investigated in greater detail in future studies. Our work suggests that, given an accurate reconstruction of the topography and underlying geology, it is possible to obtain ground shaking scenarios with realistic features, that is comparable to the recorded motions, relying on some basic data on the seismic event. The latter include the target magnitude, the hypocentral depth—which typically ranges between 7 and 10 km for crustal earthquakes in the Appennine region—and the causative fault, which is constrained by accredited databases (such as DISS). Although a rigorous statistical analysis has not been carried out, the results of this study suggest the potential use of physics-based ground shaking scenarios for generating real-time ground shaking scenarios, with relevant implications for civil protection. A more extended study, including the generation of broad-band ground motions over a wider domain (including other geological structures besides the Aterno Valley), will be the subject of a future work. Furthermore, in future analyses, the influence of the anisotropy and heterogeneity of the Earth crustal model will also be addressed.

ACKNOWLEDGMENTS

This paper is part of a larger project focused on the post-earthquake reconstruction of the city of L'Aquila (see https://www.opendatalaquila.it/).

This work was partially supported by the GNCS INdAM and the GSSI 'Centre for Urban Informatics and Modelling' (CUIM). All numerical simulations have been realized on the Linux HPC cluster Caliban of the High Performance Parallel Computing Laboratory of the Department of Information Engineering, Computer Science and Mathematics (DISIM) at the University of L'Aquila (https://caliband.disim.univaq.it), employing the software SPEED (http://speed.mox.polimi.it). We thank the DISIM for the technical support. We also thank Dr Simone Atzori (INGV) for the DInSAR data on the permanent displacement maps. Domains were partly constructed using Leapfrog [https://www.seequent.com/products-solutions/leapfrog-geo/ (Seequent 2019)].

IM, PFA and AQ are members of INdAM-GNCS; BR and PM are members of INdAM-GNAMPA. FDiM, RA and PM are members of GSSI-CUIM research centre. We also thank the two anonymous referees and the associate editor for the constructive remarks.

DATA AVAILABILITY

Numerical models and results will be available at https://www.opendatalaquila.it.

Downloaded from https://academic.oup.com/gji/article/230/1/29/6526874 by INGV user on 22 June 2022

REFERENCES

Ameri, G. *et al.*, 2009. The 6 April 2009 M_w 6.3 L'Aquila (central Italy) earthquake: strong-motion observations, *Seismol. Res. Lett.,* **80**(6), 951–966.

Ameri, G., Gallovič, F. & Pacor, F., 2012. Complexity of the M_w 6.3 2009 L'Aquila (central Italy) earthquake: 2. Broadband strong motion modeling, *J. geophys. Res.,* **117**(B4), doi:10.1029/2011JB008729.

Anderson, J.G., 2004. Quantitative measure of the goodness-of-fit of synthetic seismograms, in *Proceedings of the 13th World Conference on Earthquake Engineering,* Vancouver, BC, Canada, p. 243.

Antonietti, P.F., Mazzieri, I., Quarteroni, A. & Rapetti, F., 2012. Non-conforming high order approximations of the elastodynamics equation, *Comput. Methods Appl. Mech. Eng.,* **209,** 212–238.

Antonietti, P.F., Ayuso de Dios, B., Mazzieri, I. & Quarteroni, A., 2016. Stability analysis of discontinuous Galerkin approximations to the elastodynamics problem, *J. Sci. Comput.,* **68,** 143–170.

Antonietti, P.F., Ferroni, A., Mazzieri, I., Paolucci, R., Quarteroni, A., Smerzini, C. & Stupazzini, M., 2018. Numerical modeling of seismic waves by discontinuous spectral element methods, *ESAIM: Proc. Surv.,* **61,** 1–37.

Asimaki, D. & Mohammadi, K., 2018. On the complexity of seismic waves trapped in irregular topographies, *Soil Dyn. Earthq. Eng.,* **114,** 424–437.

Assimaki, D., Ledezma, C., Montalva, G.A., Tassara, A., Mylonakis, G. & Boroschek, R., 2012. Site effects and damage patterns, *Earthq. Spectra,* **28**(S1), S55–S74.

Atzori, S. *et al.*, 2009. Finite fault inversion of DInSAR coseismic displacement of the 2009 L'Aquila earthquake (central Italy), *Geophys. Res. Lett.,* **36**(15), doi:10.1029/2009GL039293.

Avallone, A. *et al.*, 2011. Very high rate (10 Hz) GPS seismology for moderate-magnitude earthquakes: the case of the M_w 6.3 L'Aquila (central Italy) event, *J. geophys. Res.,* **116**(B2), doi:10.1029/2010JB007834.

Balasco, M. *et al.*, 2011. Deep geophysical electromagnetic section across the middle Aterno Valley (central Italy): preliminary results after the April 6, 2009 L'Aquila earthquake, *Boll. Geofis. Teor. Appl.,* **52**(3), 443–455.

Bard, P. & Bouchon, M., 1980. The seismic response of sediment-filled valleys. Part 1. The case of incident SH waves, *Bull. seism. Soc. Am.,* **70**(4), 1263–1286.

Bertini, T. & Bosi, C., 1976. Sedimenti continentali probabilmente Pliocenici nella Valle del Salto e nella Conca del Fucino (Rieti e l'Aquila), *Ital. J. Geosci.,* **95,** 767–801.

Bertini, T. & Bosi, C., 1993. La tettonica quaternaria della conca di Fossa (L'Aquila), *Il Quaternario,* **6**(2), 293–314.

Bielak, J. *et al.*, 2010. The ShakeOut earthquake scenario: Verification of three simulation sets, *Geophys. J. Int.,* **180**(1), 375–404.

Bosi, C., 1989. Tentativo di correlazione fra le successioni pliopleistoceniche, *Elementi di tettonica pliocenico-quaternaria e indizi di sismicità olocenica nell'Appennino laziale-abruzzese,* pp. 89–96.

Bosi, C. & Bertini, T., 1970. Geologia della media valle dell'Aterno, *Mem. Soc. Geol. Ital.,* **9**(4), 719–777.

Bouchon, M. & Barker, J.S., 1996. Seismic response of a hill: the example of Tarzana, California, *Bull. seism. Soc. Am.,* **86**(1A), 66–72.

Bouchon, M., Schultz, C.A. & Toksöz, M., 1996. Effect of three-dimensional topography on seismic motion, *J. geophys. Res.,* **101**(B3), 5835–5846.

Breuer, A., Heinecke, A., Rettenberger, S., Bader, M., Gabriel, A.-A. & Pelties, C., 2014. Sustained petascale performance of seismic simulations with SeisSol on SuperMUC, in *International Supercomputing Conference,* Leipzig (Germany), pp.1–18, Springer.

Burstedde, C., Stadler, G., Alisic, L., Wilcox, L.C., Tan, E., Gurnis, M. & Ghattas, O., 2013. Large-scale adaptive mantle convection simulation, *Geophys. J. Int.,* **192**(3), 889–906.

Carafa, M. & Bird, P., 2016. Improving deformation models by discounting transient signals in geodetic data: 2. Geodetic data, stress directions, and long-term strain rates in Italy, *J. geophys. Res.,* **121**(7), 5557–5575.

Carafa, M., Valensise, G. & Bird, P., 2017. Assessing the seismic coupling of shallow continental faults and its impact on seismic hazard estimates: a case-study from Italy, *Geophys. J. Int.,* **209**(1), 32–47.

Carafa, M. *et al.*, 2020. Partitioning the ongoing extension of the central Apennines (Italy): fault slip rates and bulk deformation rates from geodetic and stress data, *J. geophys. Res.,* **125**(7).

Centamore, E., U. & Dramis, F., 2010. *Note illustrative della Carta Geologica d'Italia alla scala 1:50.000, Foglio 358- Pescorocchiano,* ISPRA-Servizio Geologico d'Italia, Ente realizzatore Regione Lazio.

Chaljub, E. *et al.*, 2015. 3-D numerical simulations of earthquake ground motion in sedimentary basins: testing accuracy through stringent models, *Geophys. J. Int.,* **201**(1), 90–111.

Cheloni, D. *et al.*, 2010. Coseismic and initial post-seismic slip of the 2009 Mw 6.3 l'Aquila earthquake, Italy, from GPS measurements, *Geophys. J. Int.,* **181**(3), 1539–1546.

Cirella, A., Piatanesi, A., Cocco, M., Tinti, E., Scognamiglio, L., Michelini, A., Lomax, A. & Boschi, E., 2009. Rupture history of the 2009 L'Aquila (Italy) earthquake from non-linear joint inversion of strong motion and GPS data, *Geophys. Res. Lett.,* **36**(19), L193041 (5 pages).

Cosentino, D. *et al.*, 2017. New insights into the onset and evolution of the central Apennine extensional intermontane basins based on the tectonically active L'Aquila Basin (central Italy), *Bulletin,* **129**(9–10), 1314–1336.

Della Seta, M., Esposito, C., Marmoni, G.M., Martino, S., Mugnozza, G.S. & Troiani, F., 2017. Morpho-structural evolution of the valley-slope systems and related implications on slope-scale gravitational processes: new results from the Mt. Genzana case history (Central Apennines, Italy), *Geomorphology,* **289,** 60–77.

De Luca, G., Marcucci, S., Milana, G. & Sano, T., 2005. Evidence of low-frequency amplification in the city of L'Aquila, Central Italy, through a multidisciplinary approach including strong-and weak-motion data, ambient noise, and numerical modeling, *Bull. seism. Soc. Am.,* **95**(4), 1469–1481.

APAT (Dipartimento Difesa del Suolo), 2005a. Italian Geological Map, sheet n° 368 "Avezzano", scale 1:50,000.

APAT (Dipartimento Difesa del Suolo), 2005b. Italian Geological Map, sheet n° 368 "L'Aquila", scale 1:50,000.

APAT (Dipartimento Difesa del Suolo), 2005c. Italian Geological Map, sheet n° 368 "Torre dei passeri", scale 1:50,000.

Dumbser, M., Käser, M. & Toro, E.F., 2007. An arbitrary high-order Discontinuous Galerkin method for elastic waves on unstructured meshes-V. Local time stepping and *p*-adaptivity, *Geophys. J. Int.,* **171**(2), 695–717.

Durand, S., Gaffet, S. & Virieux, J., 1999. Seismic diffracted waves from topography using 3-D discrete wavenumber-boundary integral equation simulation, *Geophysics,* **64**(2), 572–578.

Duru, K., Rannabauer, L., Gabriel, A.-A., Kreiss, G. & Bader, M., 2020. A stable discontinuous Galerkin method for the perfectly matched layer for elastodynamics in first order form, *Numer. Math.,* **146**(4), 729–782.

Evangelista, L. *et al.*, 2017. Physics-based seismic input for engineering applications: a case study in the Aterno river valley, Central Italy, *Bull. Earthq. Eng.,* **15**(7), 2645–2671.

Ewald, M., Igel, H., Hinzen, K.-G. & Scherbaum, F., 2006. Basin-related effects on ground motion for earthquake scenarios in the lower rhine embayment, *Geophys. J. Int.,* **166**(1), 197–212.

Ferroni, A., Antonietti, P.F., Mazzieri, I. & Quarteroni, A., 2017. Dispersion-dissipation analysis of 3-D continuous and discontinuous spectral element methods for the elastodynamics equation, *Geophys. J. Int.,* **211,** 1554–1574.

Gallipoli, M.R., Gizzi, F.T., Rizzo, E., Masini, N., Potenza, M.R., Albarello, D. & Lapenna, V., 2012. Site features responsible for uneven seismic effects in historical centre of Melfi (Basilicata, Southern Italy), *Disaster Adv.,* **5**(3), 125–137.

Galvez, P., Ampuero, J.-P., Dalguer, L.A., Somala, S.N. & Nissen-Meyer, T., 2014. Dynamic earthquake rupture modelled with an unstructured 3-D spectral element method applied to the 2011 M9 Tohoku earthquake, *Geophys. J. Int.,* **198**(2), 1222–1240.

Giaccio, B. *et al.*, 2012. Fault and basin depocentre migration over the last 2 Ma in the L'Aquila 2009 earthquake region, central Italian Apennines, *Quat. Sci. Rev.,* **56,** 69–88.

Downloaded from https://academic.oup.com/gji/article/230/1/29/6526874 by INGV user on 22 June 2022

Guidoboni, E. *et al.*, 2019. CFTI5Med, the new release of the catalogue of strong earthquakes in Italy and in the Mediterranean area, *Sci. Data,* **6**(1), 1–15.

Gutenberg, B., 1957. Effects of ground on earthquake motion, *Bull. seism. Soc. Am.,* **47**(3), 221–250.

Hailemikael, S., Lenti, L., Martino, S., Paciello, A., Rossi, D. & Mugnozza, G.S., 2016. Ground-motion amplification at the colle di roio ridge, central italy: a combined effect of stratigraphy and topography, *Geophys. J. Int.,* **206**(1), 1–18.

Improta, L. *et al.*, 2012. High-resolution controlled-source seismic tomography across the Middle Aterno basin in the epicentral area of the 2009, Mw 6.3, L'Aquila earthquake (central Apennines, Italy), *Ital. J. Geosci.,* **131**(3), 373–388.

Infantino, M., Mazzieri, I., Özcebe, A.G., Paolucci, R. & Stupazzini, M., 2020. 3D physics-based numerical simulations of ground motion in Istanbul from earthquakes along the marmara segment of the North Anatolian Fault, *Bull. seism. Soc. Am.,* **110**(5), 2559–2576.

Kastelic, V., Burrato, P., Carafa, M. & Basili, R., 2017. Repeated surveys reveal nontectonic exposure of supposedly active normal faults in the central Apennines, Italy, *J. geophys. Res.,* **122**(1), 114–129.

Kawase, H., 1996. The cause of the damage belt in Kobe: "The basin-edge effect," constructive interference of the direct S-wave with the basin-induced diffracted/Rayleigh waves, *Seismol. Res. Lett.,* **67**(5), 25–34.

Komatitsch, D., Liu, Q., Tromp, J., Suss, P., Stidham, C. & Shaw, J.H., 2004. Simulations of ground motion in the los angeles basin based upon the spectral-element method, *Bull. seism. Soc. Am.,* **94**(1), 187–206.

Kotha, S.R., Weatherill, G., Bindi, D. & Cotton, F., 2020. A regionally-adaptable ground-motion model for shallow crustal earthquakes in Europe, *Bull. Earthq. Eng.,* **18,** 4091–4125.

Lee, S.J., Komatitsch, D., Huang, B.S. & Tromp, J., 2009. Effects of topography on seismic-wave propagation: an example from northern Taiwan, *Bull. seism. Soc. Am.,* **99**(1), 314–325.

Lovati, S., Bakavoli, M., Massa, M., Ferretti, G., Pacor, F., Paolucci, R., Haghshenas, E. & Kamalian, M., 2011. Estimation of topographical effects at narni ridge (central Italy): comparisons between experimental results and numerical modelling, *Bull. Earthq. Eng.,* **9**(6), 1987–2005.

Macrì, P., Smedile, A., Speranza, F., Sagnotti, L., Porreca, M., Mochales, T. & Ermolli, E.R., 2016. Analysis of a 150 m sediment core from the co-seismic subsidence depocenter of the 2009 Mw= 6.1 L'Aquila earthquake (Italy): implications for Holocene-Pleistocene tectonic subsidence rates and for the age of the seismogenic Paganica fault system, *Tectonophysics,* **687,** 180–194.

Magnoni, F., Casarotti, E., Michelini, A., Piersanti, A., Komatitsch, D., Peter, D. & Tromp, J., 2013. Spectral-element simulations of seismic waves generated by the 2009 L'Aquila earthquake, *Bull. seism. Soc. Am.,* **104**(1), 73–94.

Mancini, M., Cavuoto, G., Pandolfi, L., Petronio, C., Salari, L. & Sardella, R., 2012. Coupling basin infill history and mammal biochronology in a Pleistocene intramontane basin: the case of western L'Aquila Basin (central Apennines, Italy), *Quat. Int.,* **267,** 62–77.

May, J., Pera, D., Di Michele, F., Rubino, B., Aloisio, R. & Marcati, P., 2021. *29th International Meshing Roundtable (IMR) (2021), Virtual Conference*. Fast CUBIT-Python Tool for Highly Accurate Topography Generation and Layered Domain Reconstruction, 184–192.

Mazzieri, I., Stupazzini, M., Guidotti, R. & Smerzini, C., 2013. SPEED: SPectral Elements in Elastodynamics with Discontinuous Galerkin: a non-conforming approach for 3D multi-scale problems, *Int. J. Numer. Method Eng.,* **95**(12), 991–1010.

Moczo, P., Kristek, J., Galis, M., Chaljub, E. & Etienne, V., 2011. 3-D finite-difference, finite-element, discontinuous-Galerkin and spectral-element schemes analysed for their accuracy with respect to P-wave to S-wave speed ratio, *Geophys. J. Int.,* **187**(3), 1645–1667.

Moczo, P., Kristek, J. & Gális, M., 2014. *The Finite-Difference Modelling of Earthquake Motions: Waves and Ruptures,* Cambridge Univ. Press.

MS-AQ Working Group , 2010. Microzonazione sismica per la ricostruzione dell'area aquilana, *Regione Abruzzo'Dipartimento della Protezione Civile, L'Aquila (in Italian)*.**3**

Nocentini, M., Asti, R., Cosentino, D., Durante, F., Gliozzi, E., M. L. & Tallini, M., 2017. Plio-Quaternary geology of L'Aquila–Scoppito Basin (Central Italy), *J. Maps,* **13**(2), 563–574.

Nocentini, M., Cosentino, D., Spadi, M. & Tallini, M., 2018. Plio-Quaternary geology of the Paganica-San Demetrio-Castelnuovo Basin (Central Italy), *J. Maps,* **14**(2), 411–420.

Paolucci, R. & Smerzini, C., 2018. Empirical evaluation of peak ground velocity and displacement as a function of elastic spectral ordinates for design, *Earthq. Eng. Struct. Dyn.,* **47**(1), 245–255.

Paolucci, R., Mazzieri, I. & Smerzini, C., 2015. Anatomy of strong ground motion: near-source records and three-dimensional physics-based numerical simulations of the Mw 6.0 2012 May 29 Po Plain earthquake, Italy, *Geophys. J. Int.,* **203**(3), 2001–2020.

Paolucci, R., Evangelista, L., Mazzieri, I. & Schiappapietra, E., 2016. The 3D numerical simulation of near-source ground motion during the Marsica earthquake, central italy, 100 years later, *Soil Dyn. Earthq. Eng.,* **91,** 39–52.

Paolucci, R., Mazzieri, I., Piunno, G., Smerzini, C., Vanini, M. & Özcebe, A.G., 2021a. Earthquake ground motion modeling of induced seismicity in the Groningen gas field, *Earthq. Eng. Struct. Dyn.,* **50**(1), 135–154.

Paolucci, R., Smerzini, C. & Vanini, M., 2021b. BB-SPEEDset: A Validated Dataset of Broadband Near-Source Earthquake Ground Motions from 3D Physics-Based Numerical Simulations, *Bull. seism. Soc. Am.* , doi:10.1785/0120210089.

Patacca, E. & Scandone, P., 1989. Post-Tortonian mountain building in the Apennines. The role of the passive sinking of a relic lithospheric slab, *The Lithosphere in Italy: Advances in Earth Science Research,* Accademia Nazionale dei Lincei, Rome,157–176

Pelties, C., Puente, J., Ampuero, J.-P., Brietzke, G. & Käser, M., 2012. Three-dimensional dynamic rupture simulation with a high-order discontinuous Galerkin method on unstructured tetrahedral meshes, *J. geophys. Res. Solid Earth,* **117**(B2), doi:10.1029/2011JB008857.

Peter, D. *et al.*, 2011. Forward and adjoint simulations of seismic wave propagation on fully unstructured hexahedral meshes, *Geophys. J. Int.,* **186**(2), 721–739.

Petersson, N.A. & Sjögreen, B., 2018. High Order Accurate Finite Difference Modeling of Seismo-Acoustic Wave Propagation in a Moving Atmosphere and a Heterogeneous Earth Model Coupled Across a Realistic Topography, *J. Sci. Comput.,* **74**(1), 209–323.

Porreca, M. *et al.*, 2016. Geological reconstruction in the area of maximum co-seismic subsidence during the 2009 Mw= 6.1 L'Aquila earthquake using geophysical and borehole data, *Ital. J. Geosci.,* **135**(2), 350–362.

Pucci, S. *et al.*, 2016. Deep electrical resistivity tomography along the tectonically active Middle Aterno Valley (2009 L'Aquila earthquake area, central Italy), *Geophys. J. Int.,* **207**(2), 967–982.

Rovida, A., Locati, M., Camassi, R., Lolli, B. & Gasperini, P., 2019. *Catalogo Parametrico dei Terremoti Italiani (CPTI15), versione 2.0*.

Schmedes, J., Archuleta, R.J. & Lavallée, D., 2013. A kinematic rupture model generator incorporating spatial interdependency of earthquake source parameters, *Geophys. J. Int.,* **192**(3), 1116–1131.

Seequent, 2018. *Leapfrog Geo v 4.5.1 [accessed 2019]*.

ISPRA, 2010a. Italian Geological Map, sheet n 358 Pescorocchiano", scale 1:50,000, ISPRA Servizio Geologico d'Italia and Regione Lazio.

ISPRA, 2010b. Italian Geological Map, sheet n 349 "Gran Sasso d'Italia", scale 1:50,000, ISPRA Servizio Geologico d'Italia and Regione Abruzzo.

Sgobba, S., Lanzano, G. & Pacor, F., 2021. Empirical nonergodic shaking scenarios based on spatial correlation models: an application to central Italy, *Earthq. Eng. Struct. Dyn.,* **50**(1), 60–80.

Smerzini, C. & Villani, M., 2012. Broadband numerical simulations in complex near-field geological configurations: The case of the 2009 M w 6.3 L'Aquila earthquake, *Bull. seism. Soc. Am.,* **102**(6), 2436–2451.

Stupazzini, M., Paolucci, R. & Igel, H., 2009. Near-fault earthquake ground-motion simulation in the Grenoble valley by a high-performance spectral element code, *Bull. seism. Soc. Am.,* **99**(1), 286–301.

Sugan, M., Kato, A., Miyake, H., Nakagawa, S. & Vuan, A., 2014. The preparatory phase of the 2009 Mw 6.3 L'Aquila earthquake by improving the detection capability of low-magnitude foreshocks, *Geophys. Res. Lett.,* **41**(17), 6137–6144.

Downloaded from https://academic.oup.com/gji/article/230/1/29/6526874 by INGV user on 22 June 2022

Tallini, M. *et al.*, 2012. Seismic surveys integrated with geological data for in-depth investigation of Mt. Pettino active Fault area (Western L'Aquila Basin), *Ital. J. Geosci.,* **131**(3), 389–402.

Tarquini, S. & Nannipieri, L., 2017. The 10 m-resolution TINITALY DEM as a trans-disciplinary basis for the analysis of the Italian territory: Current trends and new perspectives, *Geomorphology,* **281,** 108–115.

Tarquini, S., Isola, I., Favalli, M., Mazzarini, F., Bisson, M., Pareschi, M.T. & Boschi, E., 2007. TINITALY/01: a new triangular irregular network of Italy, *Ann. Geophys.,***50**(3),407–425.

Tarquini, S., Vinci, S., Favalli, M., Doumaz, F., Fornaciai, A. & Nannipieri, L., 2012. Release of a 10-m-resolution DEM for the Italian territory: Comparison with global-coverage DEMs and anaglyph-mode exploration via the web, *Comput. Geosci.,* **38**(1), 168–170.

Tromp, J., Komatitsch, D. & Liu, Q., 2008. Spectral-element and adjoint methods in seismology, *Commun. Comput. Phys.,* **3**(1), 1–32.

van Zelst, I., Wollherr, S., Gabriel, A.-A., Madden, E.H. & van Dinther, Y., 2019. Modeling megathrust earthquakes across scales: one-way coupling from geodynamics and seismic cycles to dynamic rupture, *J. geophys. Res.,* **124**(11), 11 414–11 446.

Vezzani, L., Ghisetti, F., Bigozzi, A., Follador, U. & Casnedi, R., 1998. *Carta geologica dell'Abruzzo: scala 1: 100.000,* Selca.

Wolf, S., Gabriel, A.-A. & Bader, M., 2020. Optimization and local time stepping of an ader-dg scheme for fully anisotropic wave propagation in complex geometries, in *International Conference on Computational Science,* Amsterdam, (Netherlands), pp.32–45, Springer.

Yano, T.E., Shao, G., Liu, Q., Ji, C. & Archuleta, R.J., 2014. Coseismic and potential early afterslip distribution of the 2009 Mw 6.3 L'Aquila, Italy earthquake, *Geophys. J. Int.,* **199**(1), 23–40.

Zambonelli, E., de Nardis, R., Filippi, L., Nicoletti, M. & Dolce, M., 2017. Performance of the Italian strong motion network during the 2009, L'Aquila seismic sequence (central Italy), *Geomorphology,* **281,** 108–115.

SUPPORTING INFORMATION

Supplementary data are available at *GJI* online.

Best scen.mp4
Model 1.mp4
Model 2.mp4

Please note: Oxford University Press is not responsible for the content or functionality of any supporting materials supplied by the authors. Any queries (other than missing material) should be directed to the corresponding author for the paper.

Downloaded from https://academic.oup.com/gji/article/230/1/29/6526874 by INGV user on 22 June 2022